



Structural Determinants of the Selectivity of 3-Benzyluracil-1-acetic Acids toward Human Enzymes Aldose Reductase and AKR1B10

Francesc X. Ruiz,^{*[a]} Alexandra Cousido-Siah,^[a] Sergio Porté,^[b] Marta Domínguez,^[c] Isidro Crespo,^[b] Chris Rechlin,^[d] André Mitschler,^[a] Ángel R. de Lera,^[c] María Jesús Martín,^[e] Jesús Ángel de la Fuente,^[e] Gerhard Klebe,^[d] Xavier Parés,^[b] Jaume Farrés,^[b] and Alberto Podjarny^{*[a]}

The human enzymes aldose reductase (AR) and AKR1B10 have been thoroughly explored in terms of their roles in diabetes, inflammatory disorders, and cancer. In this study we identified two new lead compounds, 2-(3-(4-chloro-3-nitrobenzyl)-2,4-dioxo-3,4-dihydropyrimidin-1(2H)-yl)acetic acid (JF0048, **3**) and 2-(2,4-dioxo-3-(2,3,4,5-tetrabromo-6-methoxybenzyl)-3,4-dihydropyrimidin-1(2H)-yl)acetic acid (JF0049, **4**), which selectively target these enzymes. Although **3** and **4** share the 3-benzyluracil-1-acetic acid scaffold, they have different substituents in their aryl moieties. Inhibition studies along with thermodynamic and structural characterizations of both enzymes revealed that the chloronitrobenzyl moiety of compound **3** can open

the AR specificity pocket but not that of the AKR1B10 cognate. In contrast, the larger atoms at the *ortho* and/or *meta* positions of compound **4** prevent the AR specificity pocket from opening due to steric hindrance and provide a tighter fit to the AKR1B10 inhibitor binding pocket, probably enhanced by the displacement of a disordered water molecule trapped in a hydrophobic subpocket, creating an enthalpic signature. Furthermore, this selectivity also occurs in the cell, which enables the development of a more efficient drug design strategy: compound **3** prevents sorbitol accumulation in human retinal ARPE-19 cells, whereas **4** stops proliferation in human lung cancer NCI-H460 cells.

Introduction

Human aldose reductase (AR, ALR2, or AKR1B1) and AKR1B10 are enzymes of biomedical interest because of their involvement in diabetes (AR) and in cancer (AR and AKR1B10). They

belong to the aldo-keto reductase superfamily (AKR) and are NADPH-dependent enzymes, folding into a highly conserved (α/β)₈ barrel. They have different substrate specificity and inhibitor selectivity due to residue differences in their three external and variable loops.^[1]

AR presents ubiquitous tissue expression and catalyzes the reduction of glucose and a wide range of aldehydes, remarkably, glutathione conjugates of lipid peroxidation products. Increased AR activity results in NADPH depletion, sorbitol accumulation, decreased cellular levels of reduced glutathione and oxidative stress,^[2] contributing to inflammation-related diseases (e.g., atherosclerosis, sepsis, asthma, colorectal carcinoma [AR inhibition prevented colon cancer metastasis in mice]).^[3] AKR1B10 shares 71% amino acid sequence identity with AR, but its tissue expression is restricted mainly to colon and small intestine. It is overexpressed in lung and liver cancers, among others, making it a potential cancer diagnostic and/or prognostic marker.^[4] AKR1B10 catalyzes the reduction of chemotherapeutic drugs, lipid peroxidation of free aldehydes and all-*trans*-retinaldehyde, but it does not catalyze the reduction of glucose.^[5] AKR1B10 may impact the carcinogenesis process through its involvement in several pathways, for example, retinoic acid signaling,^[4b,6] lipid aldehyde detoxification, and lipid synthesis.^[4c,7]

Despite the fact that a large number of AR inhibitors (ARIs) have been designed and even assayed in clinical trials, epalre-

[a] Dr. F. X. Ruiz,^{††} A. Cousido-Siah,^{*} Dr. A. Mitschler, Dr. A. Podjarny
Department of Integrative Biology
Institut de Génétique et de Biologie Moléculaire et Cellulaire
CNRS, INSERM, Uds, rue Laurent Fries, 67404 Illkirch CEDEX (France)
E-mail: fxavier.ruiz@gmail.com
podjarny@igbmc.fr

[b] Dr. S. Porté, I. Crespo, Prof. Dr. X. Parés, Prof. Dr. J. Farrés
Department of Biochemistry and Molecular Biology
Universitat Autònoma de Barcelona, 08193 Bellaterra, Barcelona (Spain)

[c] Dr. M. Domínguez, Prof. Dr. Á. R. de Lera
Departamento de Química Orgánica and
Centro de Investigaciones Biomédicas (CINBIO)
Universidade de Vigo, 363100 Vigo (Spain)

[d] C. Rechlin, Prof. Dr. G. Klebe
Institute of Pharmaceutical Chemistry
University of Marburg, Marbacher Weg 6, 35032 Marburg (Germany)

[e] Dr. M. J. Martín, Dr. J. Á. de la Fuente
Biomar Microbial Technologies S.A.
Parque Tecnológico de León, 24009 León (Spain)

[†] These authors contributed equally to this work.

[††] Present address: Center for Advanced Biotechnology and Medicine, Department of Chemistry and Chemical Biology, Rutgers University, Piscataway, NJ 08854-5627 (USA)

Supporting information for this article is available on the WWW under <http://dx.doi.org/10.1002/cmdc.201500393>.

stat (**16**) (all chemical structures apart from those involved in synthesis are shown in Scheme S1 of the Supporting Information) is the only ARI approved for therapy, although restricted to Japan, China, and India. The failure of ARIs as therapeutic agents has been mainly due to poor pharmacokinetic properties, lack of clinical efficacy, and/or unacceptable side effects.^[2a,b,8] Most ARIs can be roughly grouped in those containing: 1) a carboxylic acid moiety, or 2) a cyclic imide group. These moieties bind to the anion-binding pocket, formed by Tyr48, His110, Trp111, and the positively charged nicotinamide moiety of the cofactor. Most ARIs possess a second moiety with one or more aromatic groups, which bind into a hydrophobic subpocket of AR, bordered by Trp111, Phe122 and Leu300. This subpocket is open, due to a conformational change and is known as the specificity pocket.^[9]

Initially, the only enzyme analyzed for off-target effects of ARIs was aldehyde reductase (or AKR1A1).^[5a,10] Several studies have recently addressed the selectivity of ARIs compared with the more closely related AKR1B10. Gallego and co-workers^[6a] solved the first three-dimensional structure of AKR1B10 in complex with NADP⁺ and tolrestat (**18**); subsequently, other researchers have reported potent and selective AKR1B10 inhibitors using in vitro assays.^[11] In the last two years, additional AKR1B10 three-dimensional structures have been solved. Crystal structures of the AKR1B10 holoenzyme and of the ternary complexes with several ARIs and with AKR1B10 inhibitors were reported by the Hu group.^[12] They observed that the orientation of the Trp112 side chain is critical for the selectivity of AKR1B10 inhibitors. Meanwhile, we solved 1) the AKR1B10 V301L–fidarestat (**17**) complex,^[13] which served as the basis to explain the selectivity of **17** for AR; 2) the methylated AKR1B10K125R/V301L–**2** complex,^[1] which characterized as a novel lead a tetrafluorophenol moiety that targets both AR and AKR1B10; and 3) the methylated AKR1B10K125R/V301L–sulindac (**26**) complex, which showed that **26** and its sulfone might be a drug lead for selective AR and AKR1B10 inhibitors.^[14]

Previously, Biomar Microbial Technologies screened a library of about 2000 marine natural products and found a polybrominated diphenyl ether compound (**1**, Figure 1) from a marine sponge (*Disydea herbacea*) that showed an IC₅₀ value of 6.4 μM against AR. This hit led to the synthesis of different series of synthetic polyhalogenated compounds (such as **2**), some of which targeted both AR and AKR1B10.^[1,15]

In the search for novel ligands selective for AKR1B10, we focused our attention on compound JF0048 (**3**), which was previously shown to be selective for rat lens AR versus rat kidney aldehyde reductase.^[16] We surmised that the modification of the 3-benzyluracil-1-acetic acid scaffold through the incorporation of additional substituents at the (poly)halogenated aryl moiety, reminiscent of the sponge natural products (i.e., compound **1**, Figure 1), might shift the selectivity of the designed compound to target AKR1B10 instead.

In the present work, this assumption was indeed confirmed, as compound JF0049 (**4**) (Figure 1) was found to be selective for AKR1B10. In addition, structural insight was gained from several X-ray structures of the corresponding complexes. The

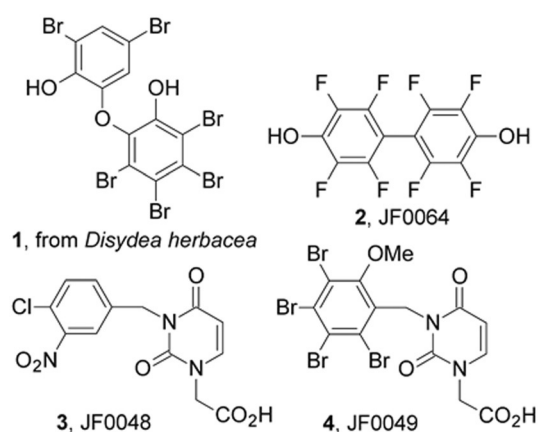


Figure 1. Structures of the polybrominated diphenyl ether compound from the marine sponge *Disydea herbacea* (2,3,4,5-tetrabromo-6-(3,5-dibromo-2-hydroxyphenoxy)phenol) (**1**), JF0064 (**2**), JF0048 (**3**), and JF0049 (**4**).

selectivity of **3** for AR was justified by its ability to open the enzyme specificity pocket, while in AKR1B10, this ligand might adopt a different conformation, resulting in weaker binding. On the other hand, the selectivity of **4** for AKR1B10 is probably due to the inability of its bulkier aryl moiety to occupy the AR specificity pocket and its improved fitting into the larger AKR1B10 active site, including a subpocket defined by loop A. This study paves the way for future efforts in structure-guided drug discovery, directed to both AR and the relatively unexplored AKR1B10.

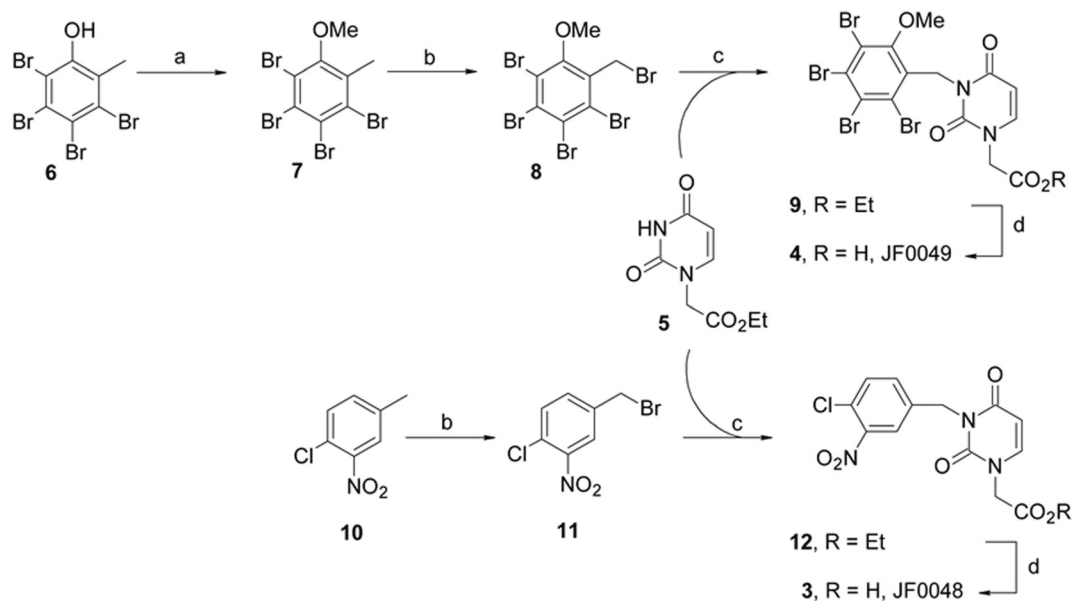
Results and Discussion

Chemistry

The synthesis of 3-benzyluracil-1-acetic acid derivatives **3** and **4** followed the methodology described for the latter compound,^[16] involving the alkylation of ethyl 2-(2,4-dioxo-3,4-dihydropyrimidin-1(2*H*)-yl)acetate **5**^[17] with the corresponding benzyl bromides **8** and **11**, respectively (Scheme 1). Benzyl bromides **8** and **11** were obtained in 96 and 47% yields, respectively, by treatment of **7** (prepared by methylation of commercially available 3,4,5,6-tetrabromocresol **6** with K₂CO₃ and MeI in acetonitrile) and **10** using bromine under photochemical irradiation conditions. A second alkylation of the monoalkylated uracil **5** with **8** and **11** using NaH in DMF provided the N,N-dialkylated uracil derivatives **9** and **12**, respectively, in 85% and 75% yield. Finally, saponification of the esters afforded the desired carboxylic acids **3** and **4**.

Inhibition assays and thermodynamic signature of AR/AKR1B10 complexes with **3** and **4**

Kotani et al.^[16] previously assayed **3** against rat lens AR and rat kidney aldehyde reductase, which were purified from the corresponding tissues. They found that **3** was one of the best hits for rat AR, with more than 4000-fold selectivity versus rat aldehyde reductase. We confirmed that **3** exhibited strong inhibi-



Scheme 1. Reagents and conditions: a) MeI, K_2CO_3 , MeCN, reflux, 4 h, 95%; b) Br_2 , CCl_4 , tungsten lamp 250 W, 90 °C, 4 h (**8**, 96%; **11**, 48%); c) NaH, DMF, 0 → 25 °C, 3 h (**9**, 85%; **12**, 75%); d) 10% NaOH, MeOH, 80 °C, 3 h (**4**, 90%; **3**, 80%).

tion against human AR ($IC_{50}=170$ nm),^[9,18] and was 127-fold and >4000-fold more potent toward human AR than toward AKR1B10 and AKR1A1, respectively. On the other hand, **4** inhibited AKR1B10 with an IC_{50} value of 450 nm, being eightfold and >200-fold more potent than for AR and AKR1A1, respectively (Table 1).

We also performed isothermal titration calorimetry (ITC) to study the binding of **3** and **4** to both enzymes. As shown in Table 2 (and Figure S1), the Gibbs free binding energy (ΔG°) and the dissociation constants (K_d) obtained by ITC were in

agreement with the inhibition assays for the binding of **3** and **4** to AR. For the binding of **4** to AKR1B10, the K_d value was slightly higher than the corresponding IC_{50} value.

Structure–activity relationships for **3** and **4** with AR and AKR1B10

With the aim of understanding the rationale behind the inhibitory properties of **3** and **4** with both AR and AKR1B10, we sought to determine the X-ray structures of the ternary complexes. We were able to obtain all except that of the AKR1B10–**3** complex. The structures folded into the expected (α/β)₈-TIM barrel, with the cofactor position conserved. Table 3 shows the data collection and refinement statistics.

Compound **3** opens the AR specificity pocket

The X-ray structure of the AR–NADP⁺–**3** complex was obtained at an atomic resolution of 1.0 Å, with the F_o-F_c omit map showing clearly the inhibitor electron density (Figure 2A). The carboxylic acid of **3** was assumed to be deprotonated, as ob-

Table 1. IC_{50} values of halogenated lead compounds.

Compd	IC_{50} [μM] ^[a]			1B10/AR	AR/1B10
	AR	AKR1B10	AKR1A1		
3	0.17 ± 0.02	21.6 ± 1.7	>100 (5.6) ^[b]	127	0.008
4	3.6 ± 0.4	0.45 ± 0.04	>100 (27.3) ^[b]	0.1	8

[a] Values are the mean ± SEM of $n=3$ independent experiments. [b] Parentheses indicate percent inhibition of AKR1A1 at 100 μM .

Table 2. Thermodynamic data of the binding events of **3** and **4** with AR and of **4** with AKR1B10.^[a]

Complex	K_d [nM]	ΔG° [kJ mol ⁻¹]	ΔH°_{obs} [kJ mol ⁻¹] ^[b]	ΔH°_{bind} [kJ mol ⁻¹] ^[c]	$-T\Delta S^\circ_{obs}$ [kJ mol ⁻¹] ^[b]	$-T\Delta S^\circ_{bind}$ [kJ mol ⁻¹] ^[c]
AR–NADP ⁺ – 3	91.1 ± 39.8	−40.4 ± 1.3	−46.7 ± 0.5	−59.7	6.1 ± 0.6	19.3
AR–NADP ⁺ – 4	8894.2 ± 1451.6	−28.8 ± 0.4	−10.7 ± 1.9	ND	−18.1 ± 1.5	ND
AKR1B10–NADP ⁺ – 3 ^[d]	ND	ND	ND	ND	ND	ND
AKR1B10–NADP ⁺ – 4	2313.3 ± 516.7	−32.2 ± 0.5	−38.7 ± 0.7	−41.6	6.0 ± 0.6	9.3

[a] Values are the mean ± SEM of $n=3$ independent experiments. [b] Thermodynamic data for the measurement in HEPES (ΔH°_{obs} and $-T\Delta S^\circ_{obs}$). [c] If possible, the values were corrected for the protonation effect (ΔH°_{bind} and $-T\Delta S^\circ_{bind}$). [d] The binding of **3** to AKR1B10 could not be measured due to the low affinity of **3** for AKR1B10. ND: not determined.

Table 3. Data collection and refinement statistics.

	AR-NADP ⁺ -3	AR-NADP ⁺ -4	AKME2MU-NADP ⁺ -4	methylylated AKR1B10 holoenzyme	AKME2MU holoenzyme
inhibitor conc. [mM]	5	5	30	–	–
PDB ID	4XZH	4XZI	4XZL	4XZM	4XZN
wavelength [Å]	0.7085	1	1.54178	0.9202	0.91907
resolution [Å]	50–1.00 (1.04–1.00)	50–2.45 (2.54–2.45)	50–1.70 (1.76–1.70)	50–1.75 (1.81–1.75)	50–1.70 (1.76–1.70)
space group	<i>P</i> 1	<i>I</i> 222	<i>P</i> 31	<i>P</i> 31	<i>P</i> 31
unit cell [Å]	46.5, 46.7, 68.3 75.0°, 78.9°, 74.4°	74.1, 84.8, 105.3 90°, 90°, 90°	79.1, 79.1, 50.2 90°, 90°, 120°	79.4, 79.4, 49.8 90°, 90°, 120°	79.9, 79.9, 50.6 90°, 90°, 120°
total reflections	390678	50932	172274	112502	129558
unique reflections	246041	22204	70350	35411	37876
multiplicity	1.6 (1.3)	2.3 (2.0)	2.4 (1.4)	3.2 (3.0)	3.4 (3.5)
completeness [%]	85.9 (73.3)	94.4 (88.4)	91.0 (66.0)	99.0 (100.0)	93.9 (94.3)
mean <i>I</i> / <i>σ</i> (<i>I</i>)	22.31 (2.44)	10.67 (2.38)	18.79 (2.77)	16.64 (2.97)	14.51 (3.36)
Wilson <i>B</i> -factor [Å ²]	8.56	43.42	23.81	25.75	25.79
<i>R</i> _{sym} ^[b]	0.028 (0.232)	0.076 (0.321) ^[a]	0.048 (0.223) ^[a]	0.065 (0.375)	0.068 (0.322)
<i>R</i> _{factor} ^[c]	0.1488	0.2188	0.2085	0.203	0.1955
<i>R</i> _{free} ^[d]	0.161	0.2895	0.2385	0.2499	0.2283
number of atoms	6175	2716	2896	2861	2908
macromolecules	5322	2579	2667	2625	2659
ligands	46	98	81	56	56
water	807	38	143	178	180
protein residues	634	316	316	316	317
RMS bonds [Å]	0.008	0.012	0.009	0.01	0.01
RMS angles [°]	1.32	1.5	1.24	1.41	1.48
Ramachandran favored [%]	97	93	98	97	97
Ramachandran outliers [%]	0	0	0	0	0
clash score	12.98	21.34	7.53	13.84	13.05
average <i>B</i> -factor [Å ²]	11.48	26.2	26.5	29.3	21.1
macromolecules	7.88	26.5	26.3	29.1	20.8
solvent	23.55	20.2	30.6	32.9	26.4

Statistics for the highest-resolution shell are shown in parentheses. [a] Anomalous pairs were treated separately. [b] $R_{\text{sym}} = \sum |I - \langle I \rangle| / \sum I$, for which *I* = observed intensity and $\langle I \rangle$ = statistically weighted average intensity of multiple observations of symmetry-related reflections. [c] $R_{\text{factor}} = \sum |F_o - |F_c|| / \sum |F_o|$, for which *F*_o = observed structure factor amplitudes and *F*_c = calculated structure factor amplitudes. [d] *R*_{free}: same definition as that for *R*_{factor} for a cross-validation set of ~5% of the reflections.

served previously for IDD594,^[19] with the oxygen atoms acting as hydrogen bond acceptors to the Tyr48 OH (2.7 Å), the His110 N_{e2} (2.7 Å), and the Trp111 N_{e1} (3.0 Å), and the creation of an electrostatic contact with the charged nicotinamide N of NADP⁺ (4.1 Å). The uracil-1-acetic acid moiety creates hydrophobic contacts with Trp20, Trp111, Trp219, and Cys298. Its aryl moiety is sandwiched between the indole moieties of Trp20 and Trp111, the latter through a face-to-face oriented π - π stacking interaction (with approximately a 3.4 Å distance between the two planes), and the side chains of Phe122, Leu300, and Cys303 lining the specificity pocket. One of the oxygen atoms of the nitro group forms a hydrogen bond with the Leu300 main chain nitrogen atom (2.9 Å), and the chlorine atom makes a halogen bond with the Thr113 OH moiety (2.9 Å) (Figure 2A).

Additionally, two non-classical hydrogen bonds are formed between the nitro oxygen atoms and the Tyr309 C_{δ1} and C_{e1} moieties (3.5 Å for both, Figure 2A), as observed for IDD393 (24) and other nitro-containing ARIs.^[20] Apparently, the sum of a halogen bond (as in the case of IDD388 [25] and 22), with the interactions provided by the nitro substituent at the *meta* position, do not trigger stronger binding. This is not surprising, taking into account that molecular interactions behave in a highly non-additive fashion.^[21]

Compound 4 is too bulky to fit into the AR specificity pocket

The X-ray structure of the AR-NADP⁺-4 complex was obtained at 2.45 Å resolution. It must be noted that crystals were obtained by co-crystallization with 5 mM of 4 in a rarely applied reservoir condition for AR crystallization, replacing the habitual ammonium citrate, pH 5.0, buffer with Tris-HCl, pH 8.0. This is the second AR structure obtained by co-crystallization at this pH, after the ternary complex of the AR holoenzyme with the inhibitor IDD552 (23) (Protein Data Bank (PDB) ID 1T41).^[22] In addition, the crystal grew in a very unusual space group, *I*222, only observed in one AR X-ray crystal structure previously, a holoenzyme complex (PDB ID 1ABN).^[23] The *F*_o-*F*_c omit map unequivocally shows the inhibitor electron density in two different conformations (A and B), where the neighboring residue (Phe122) adopts two different conformations in accordance with the inhibitor positioning (Figure 2B and 2C). Both conformations of 4 are stabilized by crystallographic contacts with the complex in the neighboring asymmetric unit. Conformation A of 4 (60% occupancy) is stabilized by the neighbor conformation A molecule, with a Br-Br contact between the two bromine atoms in *para*, while conformation B of 4 is stabilized through halogen bonds with the main chain of loop A residues of the complex in the neighboring asymmetric unit (Fig-

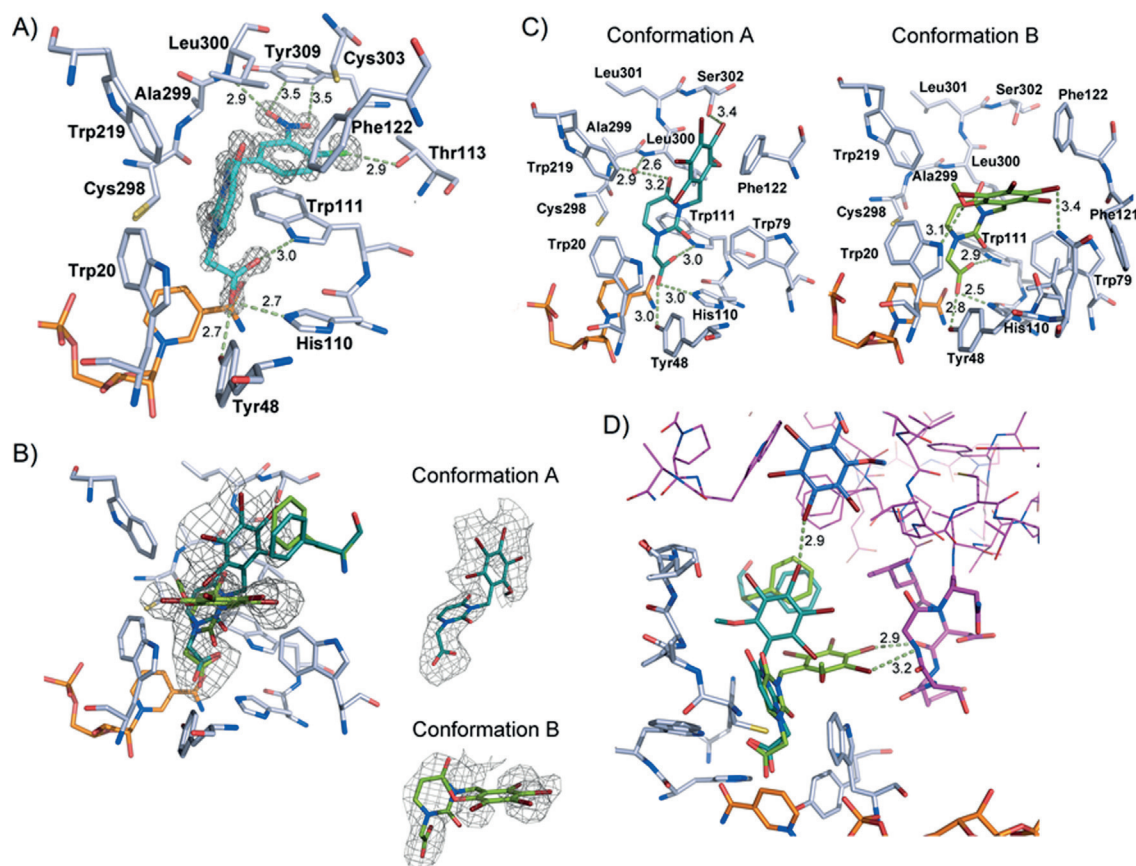


Figure 2. X-ray structures of the AR–NADP⁺–3 and AR–NADP⁺–4 complexes. A) Atomic representation of the inhibitor binding site for the AR–NADP⁺–3 complex, with the inhibitor electron density shown as a σ A-weighted $F_o - F_c$ omit map contoured at the 6σ level in grey mesh, and the protein residues, the cofactor and **3** represented as sticks (white, orange, and cyan, respectively); B) Atomic representation of the inhibitor binding site for the AR–NADP⁺–4 complex conformation ensemble, with the inhibitor electron density shown as a σ A-weighted $F_o - F_c$ omit map contoured at the 3σ level in grey mesh (with both conformations showing the inhibitor bound (top) and separated (down)), and the protein residues in white sticks (except for Phe 122, which follows the coloring of **4**), the cofactor in orange sticks, and **4** in green sticks (blue-green for conformation A, olive green for conformation B); C) Atomic representation of the inhibitor binding site for the AR–NADP⁺–4 complex, with each conformation shown in a separate drawing (for color coding, see legend for panel B); D) Atomic representation of the inhibitor binding site for the AR–NADP⁺–4 complex conformation ensemble, including the intermolecular crystallographic contacts with the symmetry-related molecules, in pink lines or sticks for the protein and in violet sticks for the symmetry-related **4**, following the same color code as for the other panels. Hydrogen bond distances are shown as green dashed lines.

ure 2D). Therefore, the observed interaction of **4** with the AR holoenzyme confirms that the conformation adopted by **3** in the cognate complex is not possible for the former compound. In this regard, we superimposed **4** in the position of **3** in its AR complex, with the methoxy group oriented toward Ala 299 or Phe 122 (Figure 3). In each case, one of the bromine atoms at the *meta* position (*ortho* to the methoxy group) would clash against the CH₂ group of Trp 79 (2.4 Å distance). For the *ortho* substituents, if the methoxy would be facing Phe 122 (Figure 3A), there would be a clash between the two groups (2.1 and 2.2 Å distance from Phe 122 C_{e2} and C_z, respectively). If the methoxy group was in the other orientation (Figure 3B), there would be steric clashes with the nitrogen and carbon atoms of the backbone of Ala 299 (2.5 Å distance).

The large aryl moiety of **4** binds in the more external hydrophobic subpocket of AKR1B10

In the case of AKR1B10, although new structures of AKR1B10–NADP⁺–inhibitor have been solved in the last two years,^[12a,24] we have only succeeded in obtaining the ternary complex with **4** in the methylated AKR1B10K125R/V301L mutant (from now on, denoted AKME2MU), as in the case of inhibitors **2** and **26**.^[1,14] The AKME2MU holoenzyme in complex with **4** was obtained at 1.70 Å resolution, with the $F_o - F_c$ omit map showing the inhibitor, and the anomalous difference map confirming the position of the four bromine atoms of compound **4** (Figure 4A). The carboxylic acid oxygen atoms display hydrogen bonds with the Tyr 49 OH (2.9 Å), His 111 N_{e2} (2.8 Å), and Trp 112 N_{e1} moieties of the conformer A (3.0 Å) (Figure 4A). The electron-deficient uracil ring is also involved in further interactions: 1) with the Trp 21 aromatic moiety through a parallel-displaced stacking (3.5 Å distance); and 2) the carbonyl oxygen

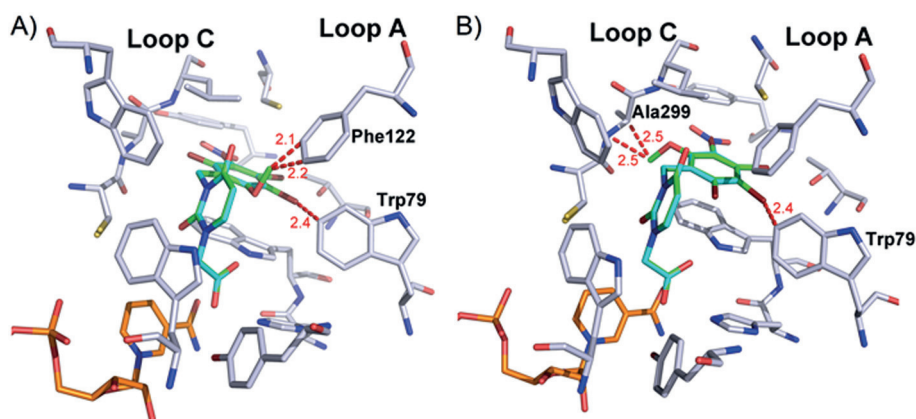


Figure 3. Steric hindrance of **4** within the AR–NADP⁺–**3** active-site conformation. Atomic representation of the inhibitor binding site for the AR–NADP⁺–**3** complex with A) **4** superimposed with the methoxy group pointing to loop A, or B) **4** superimposed with the methoxy group pointing to loop C. The protein residues, the cofactor, **3**, and **4** are shown as sticks (white, orange, cyan, and green, respectively). The short distances, demonstrating **4** steric hindrance in this AR active site conformation, are displayed as red dashed lines and red labels.

atoms are hydrogen bonded to Phe 123 C_{e1} and to Trp 220 CH₂, the two being non-classical hydrogen bonds^[20,25] (Figure 4A, atomic distances of 3.2 Å for both interactions, not shown).

The methylene bridge and the tetrabromomethoxy aryl moiety are surrounded by a hydrophobic subpocket formed by Trp 80, Trp 112, Phe 116, Phe 123, Ala 131, Leu 301 (Val 301 in the wild-type enzyme), and the aliphatic parts of Arg 125 (Lys 125 in the wild-type form) and Gln 303 (Figure 4B). The most significant interactions are the edge-to-face stacking that the aryl moiety performs with the side chain of Phe 123 (3.8 Å distance, data not shown) and the interactions of two of the bromine atoms of **4** with the aromatic ring systems of Trp 80 and Phe 116, respectively (3.5 Å in both cases, data not shown). Interestingly, Trp 112 was observed in two different conformations (Figure 4C): conformation A (flipped), with 61% occupancy and positioned as in the AKR1B10–**18** complex (PDB ID 1ZUA), and conformation B (native), with 39% occupancy and positioned as in the AKR1B10 holoenzyme structure (PDB ID 4GQG). Trp 112 conformation B is stabilized by a specific hydrogen bonding network centered on Gln 114 conformation B (58% occupancy) and including Ser 304 (Figure 4C). The latter conformation was also observed for several specific AKR1B10 inhibitors.^[12] In fact, the occupancy of **4** was found to be 64%, which might suggest that two conformations of the protein coexist in the crystal; conformation A may be that of the AKME2MU holoenzyme in complex with the inhibitor (with Trp 112 flipped), while conformation B may correspond to that of the unliganded AKME2MU holoenzyme (with Trp 112 in the native position). In addition, there is an interstitial water molecule (HOH 116) interacting with two of the Br atoms of **4** (3.3 and 3.2 Å, respectively) and with N_{e1} (2.9 Å) of conformation A of Trp 112 (Figure 4C), which is also present in conformation B, as it displays 100% occupancy and has no clashes.

Modeling the binding of **3** to AKME2MU predicts a geometric interaction similar to that of **4**

The AKME2MU–NADP⁺–**3** complex was solved, but no electron density corresponding to the inhibitor could be distinguished. We superimposed the AKME2MU–NADP⁺–**3** (PDB, MTZ, and validation files are given in the Supporting Information), and the AKME2MU holoenzyme maps (PDB ID 4XZN, Table 3 shows the data collection and refinement statistics), and it could be inferred that the former corresponds to the enzyme with the open specificity pocket (loop C open and Trp 112 in flipped conformation) (Fig-

ure S2A). Then, the obtained AKME2MU–NADP⁺–**3** coordinates, with no observable electron density for **3**, were used as a macromolecule in AutoDock 4.2^[26] in order to generate an AKME2MU–NADP⁺–**3** model. The ligand coordinates were generated by superimposing **3** to the observed **4** in the AKME2MU–NADP⁺–**4** X-ray structure. The pose chosen after the docking attempt (DLG file in the Supporting Information) was the one with the ligand ranked highest in ΔG , with the closest RMSD to the reference and with conserved hydrogen bonds between the carboxylic acid oxygen atoms and Tyr 49, His 111, and Trp 112 side chains, which is prototypical for carboxylic AR inhibitors (ARIs).^[9]

In the resulting AKME2MU–NADP⁺–**3** model, the inhibitor is bound in a similar position to that of the cognate AKME2MU–NADP⁺–**4** (Figure 5B). Indeed, the hydrogen bond pattern with the carboxylic acid groups is conserved as aforementioned, but the stacking interaction with Trp 21 is lost in the former. Furthermore, the chloronitrophenyl moiety is involved in an edge-to-face stacking interaction with the Phe 123 side chain (3.6 Å distance, data not shown), and the nitro group oxygen atoms are hydrogen bonded to Gln 303 N_{e2} on one side (2.6 Å) and to Arg 125 NH₁ (3.1 Å) in the other. A total of 135 of the 150 docking poses obtained have the nitro group in this position (Figure 5A). This conformation could not occur in AR, as Gln 303 in AKR1B10 is Ser 302 in AR, and Lys 125 in AKR1B10 (Arg 125 in the model; however, Lys 125 could also be hydrogen bonded) is Leu 124 in AR.

ITC experiments reveal a strong enthalpic contribution for the binding of **3** to AR and of **4** to AKR1B10

ITC experiments were performed to gain insight into the thermodynamic profiles of the binding events of the inhibitors to AR and AKR1B10. The binding of the carboxylate-type inhibitors to AR is accompanied by an uptake of 0.7–0.9 protons per mole of formed complex with Tyr 48.^[27] To correct for buffer de-

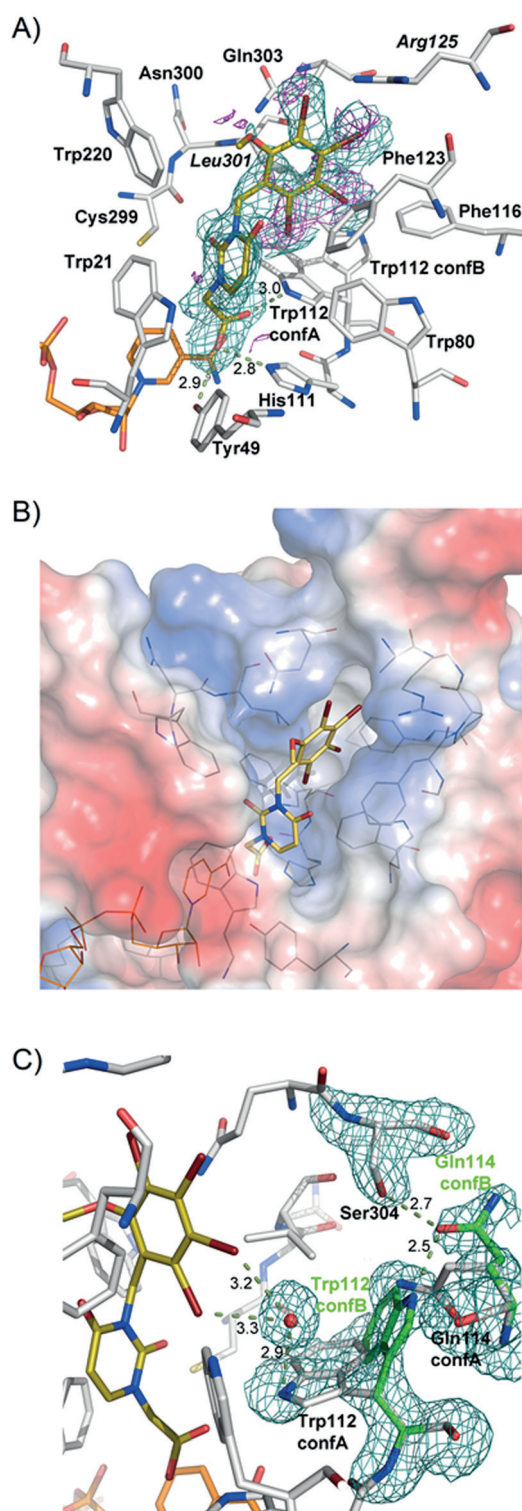


Figure 4. X-ray structure of the AKME2MU-NADP⁺-4 complex. A) Atomic representation of the inhibitor binding site for the AKME2MU-NADP⁺-4 complex, with the inhibitor electron density shown as a σ_A -weighted $F_o - F_c$ omit map contoured at the 2σ level as a cyan mesh, and as an anomalous difference map, measured on the bromine edge, contoured at the 2σ level as a purple mesh. The protein residues, the cofactor, and 4 are shown as white, orange, and gold-yellow sticks, respectively (mutated residues are labeled in italics); B) Atomic representation of the inhibitor binding site for the AKME2MU-NADP⁺-4 complex, including the surface representation, colored according to the local electrostatic potential (blue, positive charge; white, neutral; red, negative charge), calculated using PyMOL, the inhibitor binding site residues and NADP⁺ as white and orange lines, respectively, and 4 as gold-yellow sticks; C) Detail of the inhibitor binding site for the AKME2MU-NADP⁺-4 complex, following the same color code as in panel A, and including the interstitial water molecule HOH 116 as a red sphere, conformation B of Trp 112 and Gln 114 in green sticks, and the σ_A -weighted $F_o - F_c$ omit map, contoured at the 2σ level as a cyan mesh of the aforementioned water molecule, Trp 112, Gln 114, and Ser 304. Hydrogen bond distances are shown in blurred green dashed lines.

tected (Figure S4), which is in good agreement with previous results for similar ARIs. As already mentioned, the formed contacts of the nitro group in the specificity pocket are linked to a strong exothermic enthalpic signal.^[20] Presumably, these interactions are responsible for the strong enthalpic binding profile of 3 to AR. The binding of 4 to AR could only be measured in HEPES, as the enthalpic signal was too low to be evaluated in the other two buffer systems (Figure S1). Nevertheless, a buffer dependency for the binding of 4 to AR could be detected. In HEPES, the binding of 4 to AR is much less enthalpy-driven than for 3 (-10.7 vs. -46.7 kJ mol⁻¹). The binding of other carboxylate-type inhibitors to AR, as measured by us (unpublished results), showed that the enthalpic contribution necessary to be corrected for the protonation effect is between -11.5 to -14.0 kJ mol⁻¹ in HEPES. Both types of ligands—those accommodating the specificity pocket and those leaving the pocket closed—show this amount of buffer dependence in HEPES. It is assumed that the protein binding of 4 is accompanied by similar proton uptake. Even if a similar impact on the enthalpic signal is anticipated for 3, owing to proton uptake, the enthalpic term of 4 will be much smaller than that of 3. Thus, the different binding modes of 3 (addresses the specificity pocket) and 4 (leaves the specificity pocket unoccupied) with AR have a significant influence on the thermodynamic profile.

As 4 binds to AR in two alternative orientations, the interpretation of its thermodynamic profile is even more complicated. The following aspects were observed: in conformation A of 4, a water molecule is fixed, due to hydrogen bonds from the oxygen atom of the benzyluracil scaffold of 4 (3.2 Å), the nitrogen atom of the Leu300 backbone (2.6 Å), and the nitrogen of the Ala299 backbone (2.9 Å) (Figure 2C). In conformation B, a hydrogen bond between the methoxy substituent of 4 and Trp 20 (3.1 Å) can be found. The bromine atoms of 4 form contacts to the polar groups of the AR. In conformation A, such an interaction is visible with the oxygen of Ser302 and, in conformation B, with the nitrogen of Gln49. However, all of these interactions do not sum to an enthalpic contribution similar to that of the 4-chloro-3-nitro-phenyl moiety of 3. For AKR1B10,

dependencies, we performed measurements in HEPES, Tricine, and Tris buffer and plotted the measured enthalpy (H°_{obs}) against the heat of ionization (H°_{ion}) of the corresponding buffer system.^[28] The corrected thermodynamic profile of 3 to AR showed a strong favorable enthalpic contribution (-59.7 kJ mol⁻¹), while the entropic term was unfavorable ($+19.3$ kJ mol⁻¹). An entrapment of 0.6 protons per mole was de-

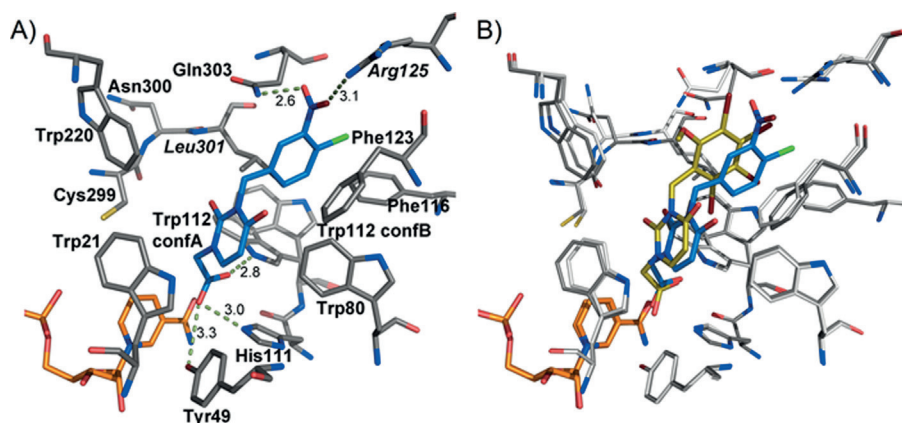


Figure 5. Model of the AKME2MU–NADP⁺–3 complex. A) Atomic representation of the inhibitor binding site for the AKME2MU–NADP⁺–3 complex, obtained by a combination of X-ray crystallography and molecular docking, with the protein residues, NADP⁺, and **3** shown as sticks (grey, orange, and blue, respectively); B) Superimposition of the AKME2MU–NADP⁺–3 complex model and the X-ray structure of the AKME2MU–NADP⁺–4 complex, with the same color code as the legend in panel A for **3** and as Figure 4 for **4**. Hydrogen bond distances are shown as blurred green dashed lines, and the mutated residues are labeled in italics.

only the binding of **4** could be measured, as the affinity of **3** toward the AKR1B10 holoenzyme was too low to be characterized by a direct ITC experiment.

Surprisingly, the measurement of **4** with AKR1B10 in the three different buffers revealed only minor buffer dependence compared with AR, as only a negligible addition of 0.1 protons per mole formed complex is detected (Figure S4). As described, Trp 112 changes from conformation B to A during binding of **4** relative to the holoenzyme. This is accompanied by a rupture of the internal hydrogen bond network, including Gln 114 and Ser304. A more profound study of the electrostatic properties of the binding pocket of AKR1B10, especially with regard to the structural changes upon ligand binding, is required to quantify the pK_a values of the local residues and their putative changes upon ligand binding to better understand this deviating behavior of AKR1B10 relative to AR. However, this example underlines the importance of studying buffer dependencies in ITC.

The thermodynamic profile of AKR1B10 binding of **4**, which was corrected for the protonation effect, showed a strong enthalpic dominance ($-41.6 \text{ kJ mol}^{-1}$), while it was accompanied by an unfavorable entropic term ($+9.3 \text{ kJ mol}^{-1}$). The enthalpic gain of the newly formed interactions between **4** and the protein clearly overcompensates for the enthalpic penalty linked to the rupture of the internal hydrogen bond network. As discussed above, we estimate the thermodynamic binding profile of **4** to AR to be much less enthalpy-dominated than for binding of **4** to AKR1B10. Accordingly, binding of **4** to AKR1B10 results in a more favorable enthalpic profile.

In summary, the comparison of binding of **3** and **4** to AR and the binding of **4** to AR and AKR1B10 indicate that the opening and accommodation of the specificity pocket lead to an enthalpic advantage. For the binding of **3** to AR, the interactions formed inside the specificity pocket seem to be responsible for the strong exothermic signal. For the binding of

4 to AKR1B10, the displacement of a water molecule might also contribute to the enthalpic signature, as will be discussed in the following section.

Desolvation costs between holoenzymes may contribute to differences in binding affinities

The modeled binding of **3** to AKME2MU has a similar geometry to that of **4**, while their inhibitory potency is quite different. Thus we decided to perform docking and thermodynamic analyses of the binding events to determine the underlying reasons for this discrepancy. First, we wished to assess the effect of the V301L and K125R mutations, which were required to obtain

the crystal structure of AKR1B10 complexed to **4**.^[1] The K125R mutation does not involve major changes regarding the active site conformation (Figure S3). As for the V301L mutation, the superimposition of all deposited AKR1B10 wild-type (Val301) and V301L mutant structures (Leu301, equivalent to Leu300 in AR) show that, while the side chains of Leu301 mainly point to the active site, Val301 side chains point to the solvent (Figure S3). The mutation also changes the orientation of the neighboring residues Leu302 and Gln303, because the larger Leu301 is fixed by a hydrophobic interaction with the side chain of Trp112 in the flipped conformation that does not occur in the AKR1B10 wild-type complexes with the smaller Val301, which moves toward the solvent. This particular effect of residue 301 was previously noticed for the AKR1B10 wild-type holoenzyme–NADP⁺–**2** model obtained by molecular dynamics (MD) simulations.^[1] Clearly, inhibitor binding is also able to induce this contact by means of the opening of the specificity pocket (AKR1B10–**18**, PDB ID 1ZUA).

As an alternative to the more time-consuming MD analyses, we inspected the available AKR1B10 wild-type structures complexed with inhibitors in the PDB and we found three main conformations: 1) AKR1B10–**18** (PDB ID 1ZUA), with a more externally oriented pocket; 2) AKR1B10–caffeic acid phenethyl ester (**21**) (PDB ID 4GQ0), very similar to the AKR1B10 holoenzyme pocket (PDB ID 4GQG) and to complexes with flufenamic acid (**20**) and **16**, (PDB IDs 4I5X and 4JIH, respectively); and 3) AKR1B10–zopolrestat (**19**) (PDB ID 4JII), with a more buried specificity pocket. Next, we docked compounds **3** and **4** into each of the three different holoenzyme conformations as receptors, but we used FlexX^[29] instead of AutoDock 4.2,^[26] as the latter has proven to be influenced by the starting conformation.^[30]

In the case of **4**, it can be observed that the inhibitor can only access the protein in the conformation found in 1ZUA (see docking in mol2 files in the Supporting Information). The

superimposition of this pose with the crystal structure of the AKME2MU–NADP⁺–4 complex shows that both are very similar (Figure S2B), thus validating the latter structure as a reliable starting point for structure-based drug design (SBDD). In the case of **3**, only the conformation found in 4GQ0 was unable to accommodate the inhibitor (see docking in mol2 files in the Supporting Information). The 4JII conformer displays **3** bound in a very similar geometry to the cognate AR–NADP⁺–3 complex (Figure S2C). However, while the AR complex provides the chlorine atom of **3** with a halogen bond acceptor (Thr113), AKR1B10 would not, as the larger Gln114 might rearrange its side chain conformation away from the chlorine to avoid a mutual clash (see PDB ID 4JII for further clarity). The 1ZUA conformer binds **3** in a more similar fashion to that of the AKME2MU–NADP⁺–3 model, but the inhibitor leans significantly closer to loop C than in the model (like reference ligand **18**), losing the stacking to Phe123. Thus, several conformations could exist for the AKR1B10 holoenzyme–**3** complex. However, given the flexible nature of the loop C–loop A region in AKR1B10, in the same fashion as in AR, the energetic cost would be likely moderate and could be compensated,^[31] probably discarding it as a cause of the different binding affinities of **3** and **4** toward AKR1B10.

The binding thermodynamics are another aspect worthy of consideration. Apart from the experimentally determined energetic terms (Table 2), it is important to consider the ligand and the protein prior to complex formation, the formed protein–ligand complex, and all changes that occur with water molecules and the various components solvated in the water environment. It is known that desolvation costs sometimes can be responsible for the strongly decreased potency of some ligands, even though they seem to fit well into a binding site.^[32] In our case, we applied the HYDE scoring function^[33] with the two AKR1B10–**3/4** complexes (obtained using the PDB files of the model and the X-ray structure, respectively, mutated in silico with Coot^[34] to the wild-type AKR1B10). HYDE considers the contribution of hydrogen bonds and dehydration energies in protein–ligand complexes and estimates the free binding energy.^[35] HYDE data indicate that **3** would suffer from a large desolvation penalty because of the oxygen atom of the nitro group facing loop C, which could explain its low affinity (see Table S1 in the Supporting Information): the oxygen atom of the nitro group would provoke its hydrogen bonding partner Gln303 side chain amide nitrogen atom to remain poorly desolvated (Figure 5A). Using HYDE, the calculated Gibbs free energy values for binding to AKR1B10 gave K_d values of 2.9 μM (similar to the experimental K_d value of 2.3 μM , Table 2) and 132 μM for **4** and **3**, respectively, a 45-fold difference. This is roughly the same difference between the experimental IC_{50} values (48-fold difference); thus, the computed HYDE score serves as a qualitative value to explain the difference in potency.

We expected the hydrophobic methoxytetrabromobenzyl moiety of **4** to entail binding to AKR1B10 with a predominantly entropic signature. However, to our surprise, the thermodynamic profile of **4**, corrected for the small protonation effect, was mainly enthalpy-driven (Table 2). The hydrophobic effect is

assumed to be entropy-driven, but it has been shown in several cases that displacement of disordered water molecules from a hydrophobic pocket can also create an enthalpic signature.^[36] Indeed, the region located at the base of loop A in AKR1B10 presents a loosely packed subpocket that is able to trap a water molecule, as discovered in the AKR1B10V301L–NADP⁺–**17** complex (and also observed in other ternary complexes, PDB IDs: 1ZUA, 4JII, and 4WEV), deviating from AR, which presents a well-packed hydrophobic subpocket.^[13] The analysis of the AKR1B10 holoenzymes crystallized by us and others (PDB IDs: 4GQG, 4XZM, and 4XZN) also showed this buried water molecule (Figure 6). The absence of other water molecules nearby suggests that this subpocket is insufficiently hydrated; that is, in spite of available space, no other water molecules are crystallographically observed, possibly meaning that they will be highly mobile and disordered. In the AKME2MU–NADP⁺–**4** complex, the inhibitor is able to displace this water molecule upon binding (Figure 6C), along with the other disordered water molecules. Their release should not contribute significantly to a large entropy gain; instead, new hydrogen bonds can be formed with other water molecules in the bulk phase which may add a significant enthalpic benefit, reflected in ITC experiments (Table 2). In the case of the AKME2MU–NADP⁺–**3** complex model, this water molecule is even closer (less than 2 Å, Figure 6C). Therefore, the low affinity of **3** for AKR1B10 could be due to the incapability of displacing this observed water molecule, or the new interactions formed (i.e., the hydrogen bond between the oxygen of the nitro group with the carboxamide nitrogen of the Gln303 side chain) may cancel out the enthalpic gain of displacing this water molecule.

Inhibition of the biological activity of AR and AKR1B10 by **3** and **4** in cellular models

To test the intracellular inhibitory potency of **3** and **4**, we used two different approaches. First, we compared their ability to prevent sorbitol accumulation within human retinal ARPE-19 cells cultured in a medium supplemented with 50 mM glucose, reproducing the typical hyperglycemic conditions of diabetes, in which AR is overexpressed.^[15b,37] The IC_{50} values for sorbitol accumulation (Table 4) were in accordance with the recombinant protein inhibition assays, as **3** prevented half of sorbitol accumulation at 0.6 μM , while **4** only succeeded at 16 μM .

Table 4. Inhibitory activity on sorbitol accumulation in human ARPE-19 retinal cells.

Compound	IC_{50} [μM] ^[a]
1 ^[b]	3
2	0.4
3	0.6
4	16
18 ^[b]	0.02

[a] Compound concentration required to inhibit sorbitol accumulation by 50%; all values are the mean of at least three experiments. [b] Determined previously by de la Fuente et al.^[15a]

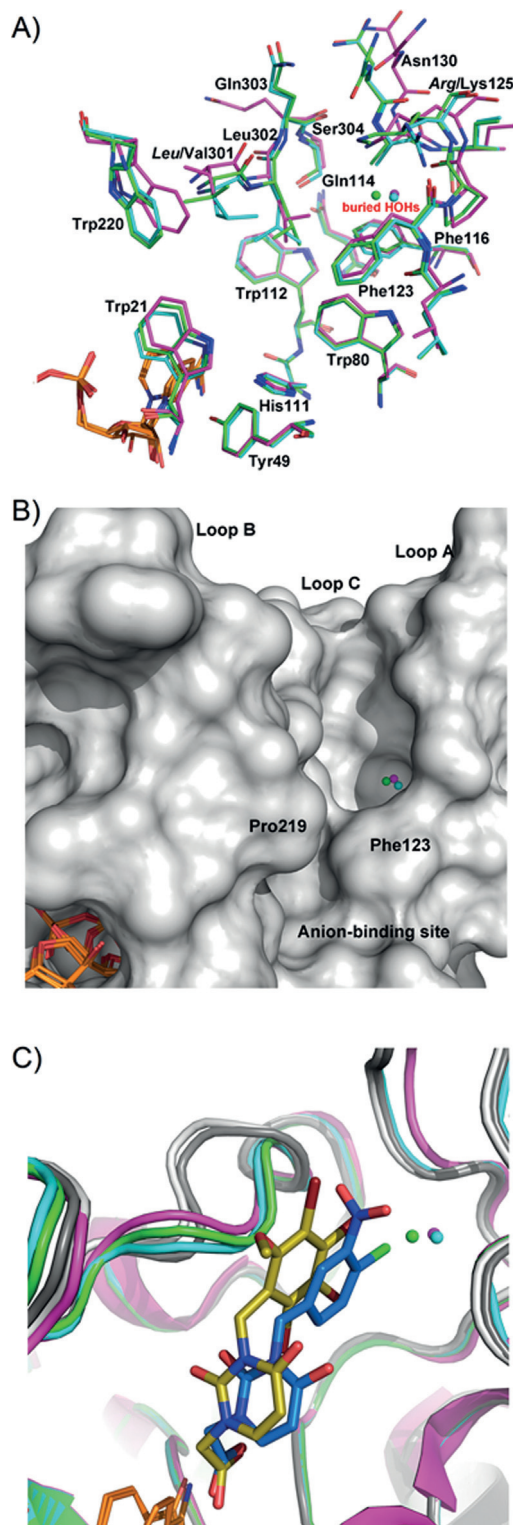


Figure 6. Impact of a crystallographically observed buried water molecule in a subpocket of the AKR1B10 holoenzyme active site on the binding of **3** and **4**. A) Superimposition of the holoenzyme X-ray structures of wild-type AKR1B10 (PDB ID 4GQG), methylated wild-type AKR1B10 (PDB ID 4XZM), and AKME2MU (PDB ID 4XZN), with the cofactor in orange sticks and the buried water molecule in pink, green, and cyan sticks and spheres, respectively (mutated residues are labeled in italics); B) Superimposition of the buried water molecules of the aforementioned AKR1B10 holoenzymes with the protein represented as a light grey surface; C) Superimposition of the holoenzyme structures with the buried water molecule and the AKME2MU-NADP⁺-3/AKME2MU-NADP⁺-4 complexes, with the protein represented as a cartoon, following the same color code for all structures. The mutated residues are labeled in italics.

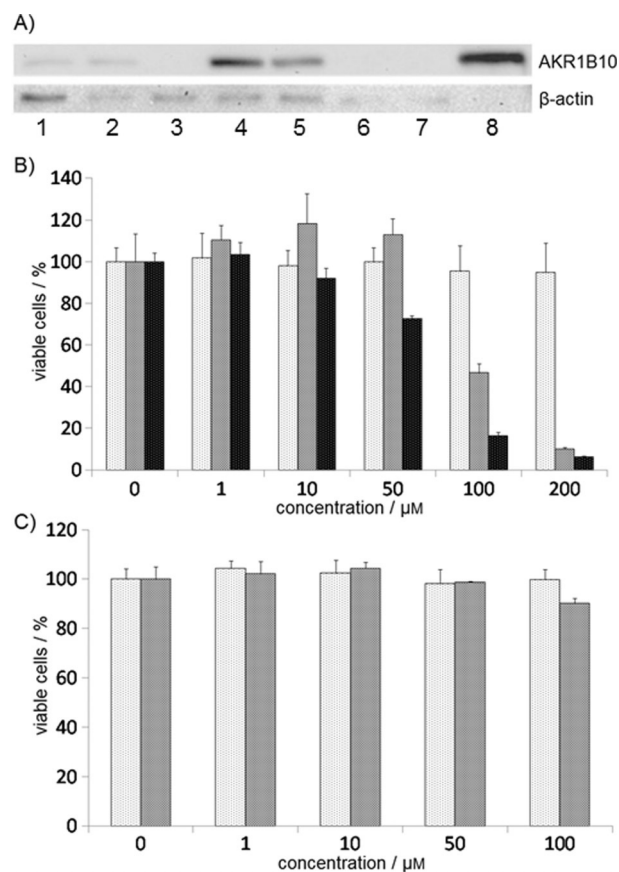


Figure 7. Effect of compounds **3** and **4** on cell viability. A) Western blot analysis of several human cell lines against AKR1B10 and β -actin (loading control). Lanes 1–7: total cell extracts from NCI-H460 (non-small cell lung carcinoma, NSCLC), HepG2 (hepatocellular carcinoma), HCT-116 (colorectal carcinoma), BT-20 (mammary gland carcinoma), A549 (NSCLC), BEAS-2B (non-tumor bronchial epithelium), and HEK293T (embryonic kidney), respectively. Purified recombinant AKR1B10 (200 ng) was used as a positive control (lane 8). B),C) Bar graphs showing the percentage of NCI-H460 (B) and BEAS-2B (C) cell viability at increasing concentrations (0–200 μ M) of inhibitor: **3** (light gray bars), **4** (dark gray bars), **16** (black bars). Bars indicate the mean \pm standard error of at least four determinations.

Secondly, to assess the degree of inhibition of **3** and **4** against AKR1B10 biological activity, we determined the effect of each compound on NCI-H460 and BEAS-2B cell viability (Figure 7). Western blot analysis showed that several tumor cell lines express AKR1B10, while non-tumor BEAS-2B cells did not (Figure 7A). NCI-H460 and BEAS-2B cells were chosen for inhib-

itor studies, as both are derived from human lung tissue. In NCI-H460 cells, a good correlation with the in vitro enzymatic inhibition tests was observed: cell viability was decreased to less than 50% with 100 μ M of **4**, while concentrations higher than 200 μ M of **3** did not have any effect (Figure 7B). To link the effect of compounds on cell viability to the in vitro

AKR1B10 inhibition, we tested **3** and **4** in the BEAS-2B cell line, a non-tumor human lung cell line. Our results show that **3** and **4** did not affect cell viability up to 100 μM (Figure 7C).

Conclusions

A large number of ARIs have been developed for the treatment of diabetic complications, with huge amounts of preclinical and clinical data collected through academic and industrial programs. In the last ten years, AKR1B10 has been shown to be overexpressed in a plethora of different cancers and has emerged as a protein related to tumorigenesis. Additionally, AR has been established as an important mediator in oxidative stress and inflammation-related processes, including colon cancer.^[38] Both AR and AKR1B10 siRNA knockdown or drug inhibition decreased tumor growth of several cell line xenografts (from different tissues) transplanted into immune-deficient mice.^[39] Therefore, AR and AKR1B10 inhibitors may represent a novel class of antitumor agents, and the clinical data assembled in diabetes clinics may ease the transition of these inhibitors to cancer chemotherapy, that is, drug repositioning (reviewed in ref. [40]).

Here, starting from the structure of uracilacetic acid **3**, we developed and synthesized compound **4**, inspired by the halogenated biaryls and diaryl ethers present in natural products. The inhibition assays, ITC experiments, X-ray crystallographic determinations, and *in silico* structural analysis of holoenzyme-**3/4** complexes enabled determination of AR and AKR1B10 selectivity and potency. The increased volume of the aryl moiety of **4** shifts the selectivity to AKR1B10, and the smaller aryl group of **3** is able to open the AR buried specificity pocket, while the bulky substituents at the *ortho* and *meta* positions of **4** prevent binding in this pocket. Conversely, the large aryl moiety of **4** enables binding into a more external subpocket in AKR1B10. The modeled binding of **3** to AKR1B10 is similar to that of **4**, but the nitro group of **3** might prevent proper binding to AKR1B10. We hypothesize that binding of **3** would imply a large desolvation penalty to the neighboring Gln303 residue because of the repulsive interaction with one of the nitro oxygen atoms, thus explaining its low affinity.

The ITC data showed that the binding of both **3** to AR and **4** to AKR1B10 display large enthalpic signatures. In the first case, the presence of the nitro group in **3** and its interactions with the open AR specificity pocket might explain the high binding enthalpy to AR (as previously observed for **24**). In the second case, compound **4** might additionally displace a disordered water molecule trapped in the AKR1B10 holoenzyme in the aforementioned subpocket at the base of loop A, creating the overall observed large enthalpic signature. Additionally, both enzymes exhibit different proton uptake upon inhibitor binding, unveiling the difference in electrostatic properties between the active sites of the two enzymes.

Remarkably, the selectivity of **3** for AR and of **4** for AKR1B10 observed in recombinant protein inhibition assays correlated well with the biological activity tests under cellular conditions. Thus, the striking differences found here could be exploited to develop selective and potent AR and AKR1B10 inhibitors, with

potential application for targeting the aforementioned pathologies.

Experimental Section

Chemistry

General. All chemicals (purchased from Sigma-Aldrich, Acros, Fluka, and Merck) were used as received unless otherwise noted. All non-aqueous reactions were performed in flame-dried glassware under an argon atmosphere. Acetone and CCl_4 were dried prior to use at reflux over CaH_2 . DMF, MeCN, and MeOH were dried using a Pure Solv Innovative Technology apparatus. Column chromatography was performed on Merck silica gel 60 (0.040–0.063 mm). Thin-layer chromatography (TLC) analysis was performed on aluminum TLC sheets (Merck, silica gel 60, F_{245}) and glass TLC plates (Merck, RP-18F_{254s}). The compounds were visualized by UV_{245nm} or spraying with phosphomolybdic acid solution, followed by heating. ^1H and ^{13}C NMR spectra were recorded on a Bruker AV 400 spectrometer (400 MHz and 100 MHz, respectively). NMR spectra were recorded in CDCl_3 , CD_2Cl_2 , CD_3OD , or $(\text{CD}_3)_2\text{SO}$. Chemical shifts (δ) are given in parts per million (ppm) and were referenced to residual solvent peaks as an internal standard. Coupling constants (J) are given in Hertz (Hz). The proton spectra are reported as follows: δ (multiplicity, coupling constant J , number of protons). DEPT135 was used to aid in the assignment of signals in the ^{13}C NMR spectra. Additional COSY and HSQC spectra were recorded in particular cases to enable interpretation of ^1H NMR data. Electron impact ionization (EI) mass spectra were recorded on a VG-autospec M instrument. For electrospray ionization (ESI), an APEX III FT-ICR MS (Bruker Daltonics, Billerica, MA), equipped with a 7T actively shielded magnet was used, and ions were generated using an Apollo API ESI source, with voltage between 1800 and 2200 V (to optimize ionization efficiency) applied to the needle and a counter voltage of 450 V applied to the capillary. The ESI spectra samples were prepared by adding a spray solution of 70:29.9:0.1 (v/v/v) MeOH/ H_2O /formic acid to a solution of the sample at a v/v ratio of 1 to 5% to give the best signal-to-noise ratio. IR spectra were recorded on a Jasco FT/IR-4200 spectrophotometer and are reported in cm^{-1} .

1,2,3,4-Tetrabromo-5-methoxy-6-methylbenzene (7): Iododethane (0.88 mL, 14.16 mmol) was added to a solution of 2,3,4,5-tetrabromo-6-methylphenol **6** (5.0 g, 11.8 mmol) and K_2CO_3 (4.89 g, 35.4 mmol) in MeCN (47.2 mL), and the mixture was stirred at reflux for 4 h. The reaction mixture was cooled to room temperature and extracted with Et_2O (3×100 mL). The combined organic layers were dried (Na_2SO_4), filtered, and concentrated. The residue was purified by column chromatography (silica gel, hexanes) to afford 4.93 g (95%) of **7** as a white solid: mp: 138–140 °C (EtOH); ^1H NMR (400 MHz, CDCl_3): δ = 3.78 (s, 3H), 2.47 ppm (s, 3H); ^{13}C NMR (100 MHz, CDCl_3): δ = 155.6 (s), 134.4 (s), 128.1 (s), 126.2 (s), 124.5 (s), 121.3 (s), 60.6 (q), 19.6 ppm (q); HRMS (TOF-EI): calcd for $\text{C}_8\text{H}_6^{79}\text{Br}_2^{81}\text{Br}_2\text{O}$ ($[M]^+$), 437.7111; found, 437.7121; IR: $\tilde{\nu}$ = 2935 (w, C–H), 2845 (w, C–H), 1439 (m), 1361 (s), 1338 (s), 1151 cm^{-1} (m).

1,2,3,4-Tetrabromo-5-(bromomethyl)-6-methoxybenzene (8): Bromine (0.471 mL, 9.13 mmol) was slowly added over 5 min to a solution of compound **7** (2.0 g, 4.57 mmol) in CCl_4 (11.14 mL). The mixture was heated at 90 °C and irradiated with a tungsten lamp (250 W) for 4 h. The mixture was washed with an aqueous solution of $\text{Na}_2\text{S}_2\text{O}_3$ (3×30 mL). The organic layer was dried (Na_2SO_4), filtered, and concentrated. The residue was purified by column chro-

matography (silica gel, hexanes) to afford 2.27 g (96%) of **8** as a pale-yellow solid: mp: 126–129 °C (hexane/EtOAc); ¹H NMR (400 MHz, CDCl₃): δ = 4.76 (s, 2H), 4.01 ppm (s, 3H); ¹³C NMR (100 MHz, CDCl₃): δ = 155.0 (s), 133.9 (s), 130.1 (s), 128.0 (s), 125.6 (s), 121.8 (s), 61.7 (t), 29.6 ppm (q); HRMS (TOF-ESI): calcd for C₉H₅⁷⁹Br₃⁸¹Br₂O ([M]⁺), 515.6172; found, 515.6233; IR: $\tilde{\nu}$ = 2935 (w, C–H), 2846 (w, C–H), 1531 (m), 1359 (s), 1343 (s), 1219 cm⁻¹ (m); UV (MeOH): λ_{max} = 226 nm.

Ethyl 2-(2,4-dioxo-3-(2,3,4,5-tetrabromo-6-methoxybenzyl)-3,4-dihydropyrimidin-1(2H)-yl)acetate (9): A solution of ethyl 2-(2,4-dioxo-3,4-dihydropyrimidin-1(2H)-yl)acetate (**5**)^[17] (0.058 g, 0.29 mmol) was added to a cold (0 °C) suspension of NaH (0.014 g, 0.36 mmol) in DMF (0.75 mL). After stirring for 1.5 h at 0 °C, a solution of **8** (0.15 g, 0.29 mmol) in DMF (1.75 mL) was added, and the mixture was stirred for 2 h at 0 °C and then for 1 h at room temperature. The mixture was poured into H₂O and extracted with EtOAc (3 × 25 mL). The combined organic layers were washed with brine (3 × 15 mL), dried (Na₂SO₄), filtered, and concentrated. The residue was purified by column chromatography (silica gel, CH₂Cl₂/MeOH, 98:2) to afford 0.156 g (85%) of **9** as a mixture of rotamers in a 5:1 ratio as a pale-yellow solid: mp: 148–150 °C (hexane/EtOAc); (major) ¹H NMR (400 MHz, CDCl₃): δ = 7.09 (d, *J* = 7.9 Hz, 1H), 5.81 (d, *J* = 7.9 Hz, 1H), 5.42 (s, 2H), 4.45 (s, 2H), 4.25 (q, *J* = 7.4 Hz, 3H), 3.86 (s, 3H), 1.29 ppm (t, *J* = 7.4 Hz, 3H); (minor) ¹H NMR (400 MHz, CDCl₃): δ = 7.43 (d, *J* = 7.2 Hz, 1H), 5.94 (d, *J* = 7.2 Hz, 1H), 5.64 (s, 2H), 4.63 (s, 2H), 4.29 (q, *J* = 7.2 Hz, 2H), 3.88 (s, 3H), 1.34 ppm (t, *J* = 7.2 Hz, 3H); HRMS (ESI⁺): calcd for C₁₆H₁₅⁷⁹Br₄N₂O₅ ([M+H]⁺), 630.7709; found, 630.7705; IR: $\tilde{\nu}$ = 2980 (w, C–H), 1745 (m, C=O), 1709 (m, C=O), 1656 (s, C=O), 1450 (m), 1352 (m), 1200 (m), 999 cm⁻¹ (m).

2-(2,4-Dioxo-3-(2,3,4,5-tetrabromo-6-methoxybenzyl)-3,4-dihydropyrimidin-1(2H)-yl)acetic acid (4): A 10% aqueous solution of NaOH (0.12 mL) was added to a solution of **9** (0.075 g, 0.12 mmol) in MeOH (3.54 mL), and the mixture was stirred at 80 °C for 3 h. The mixture was cooled to room temperature, acidified with 10% HCl, and extracted with EtOAc (3 × 10 mL). The combined organic layers were dried (Na₂SO₄), filtered, and concentrated. The residue was purified by recrystallization from EtOH to afford 0.065 g (90%) of **4** as a white solid: mp: 227–230 °C (EtOH); ¹H NMR (400 MHz, CD₃OD): δ = 7.33 (d, *J* = 7.9 Hz, 1H), 5.74 (d, *J* = 7.8 Hz, 1H), 5.37 (s, 2H), 4.45 (s, 2H), 3.80 ppm (s, 3H); ¹³C NMR (100 MHz, CDCl₃): δ = 169.8 (s), 164.0 (s), 156.8 (s), 151.9 (s), 144.3 (d), 132.6 (s), 129.1 (s), 127.7 (s), 125.6 (s), 121.9 (s), 101.7 (d), 61.9 (q), 50.1 (t), 43.9 ppm (t); HRMS (TOF-ESI⁺): calcd for C₁₄H₁₁⁷⁹Br₄N₂O₅ ([M+H]⁺), 602.7396; found, 602.7424; IR: $\tilde{\nu}$ = 3500–3000 (br, OH), 2922 (w, C–H), 1709 (s, C=O), 1660 (s, C=O), 1457 (m), 1361 cm⁻¹ (m); UV (MeOH): λ_{max} = 269, 220 nm.

4-(Bromomethyl)-1-chloro-2-nitrobenzene (11): According to the procedure described above, compound **10** (1.5 g, 8.74 mmol) in CCl₄ (21.3 mL) was treated with Br₂ (0.896 mL, 17.48 mmol), heated at 90 °C, and irradiated with a tungsten lamp (250 W) for 6 h. Purification of the residue by distillation afforded 0.772 g (51%) of starting material and 1.05 g (48%) of **11** as a yellow oil. Spectroscopic data matched those described in the literature.^[8b]

Ethyl 2-(3-(4-chloro-3-nitrobenzyl)-2,4-dioxo-3,4-dihydropyrimidin-1(2H)-yl)acetate (12): Following the procedure detailed above, from ethyl 2-(2,4-dioxo-3,4-dihydropyrimidin-1(2H)-yl)acetate **5**^[17] (0.336 g, 1.69 mmol) and 4-(bromomethyl)-1-chloro-2-nitrobenzene **11** (0.42 g, 1.66 mmol) in DMF (10 mL), ethyl 2-(3-(4-chloro-3-nitrobenzyl)-2,4-dioxo-3,4-dihydropyrimidin-1(2H)-yl)acetate **12** (0.459 g, 75%) was obtained, after purification by column chromatography

(silica gel, from 100:0 to 99:1 CH₂Cl₂/MeOH) and crystallization (mp: 117–118 °C, hexane/EtOAc). The spectroscopic data matched those described in the literature.^[8b] ¹H NMR (400 MHz, CD₂Cl₂): δ = 7.92 (d, *J* = 1.9 Hz, 1H), 7.62 (dd, *J* = 8.3, 2.0 Hz, 1H), 7.49 (d, *J* = 8.3 Hz, 1H), 7.13 (d, *J* = 7.9 Hz, 1H), 5.79 (d, *J* = 7.9 Hz, 1H), 5.10 (s, 2H), 4.44 (s, 2H), 4.21 (q, *J* = 7.1 Hz, 2H), 1.25 ppm (t, *J* = 7.1 Hz, 3H); ¹³C NMR (100 MHz, CD₂Cl₂): δ = 167.3 (s), 162.4 (s), 151.4 (s), 147.8 (s), 143.0 (d), 137.4 (s), 133.8 (d), 131.7 (d), 125.9 (d), 125.8 (s), 101.9 (d), 62.2 (t), 50.0 (t), 43.0 (t), 13.8 ppm (q).

2-(3-(4-Chloro-3-nitrobenzyl)-2,4-dioxo-3,4-dihydropyrimidin-1(2H)-yl)acetic acid 3. Following the procedure detailed above, from ethyl 2-(3-(4-chloro-3-nitrobenzyl)-2,4-dioxo-3,4-dihydropyrimidin-1(2H)-yl)acetate **12** (0.1 g, 0.27 mmol), 2-(3-(4-chloro-3-nitrobenzyl)-2,4-dioxo-3,4-dihydropyrimidin-1(2H)-yl)acetic acid **3** (0.073 g, 80%) it was obtained, after purification by crystallization from EtOH (mp: 183–184 °C). The spectroscopic data matched those reported in the literature.^[8b] ¹H NMR (400 MHz, (CD₃)₂CO): δ = 7.97 (d, *J* = 1.7 Hz, 1H), 7.66 (d, *J* = 8.0 Hz, 1H), 7.7–7.6 (m, 2H), 5.79 (d, *J* = 7.8 Hz, 1H), 5.14 (s, 2H), 4.62 ppm (s, 2H); ¹³C NMR (100 MHz, (CD₃)₂CO): δ = 169.4 (s), 163.3 (s), 152.4 (s), 148.8 (s), 145.3 (d), 139.3 (s), 134.3 (d), 132.4 (d), 126.1 (d), 125.3 (s), 101.5 (d), 50.3 (t), 43.4 ppm (t).

Protein purification, crystallography, and biological assays

Site-directed mutagenesis, enzyme expression, and purification. cDNAs of AR and AKR1A1 were subcloned into the pET15b plasmid, while cDNA of AKR1B10 was subcloned into the pET16b plasmid (pET30-Xa/LIC was used for the K125R/V301L mutant). AR, wild-type and mutant AKR1B10, and AKR1A1 were recombinantly expressed in the *E. coli* BL21(DE3) strain (Novagen) and were purified using the procedures described previously for AR,^[41] AKR1B10,^[6a] and AKR1A1.^[42] Purity was confirmed by SDS-PAGE, and protein concentration was determined using a NanoDrop ND-1000 (Thermo Scientific).

Inhibitor screening. The IC₅₀ activity assays were carried out according to the quantification of NADPH consumption, which takes place when the enzyme catalyzes the conversion of D,L-glyceraldehyde into glycerol. The assays were performed at 25 °C in 100 mM sodium phosphate buffer, pH 7.0, with a protein amount equivalent to the V_{max} and 0.2 mM NADPH. The final reaction volume was 500 μL. All compounds assayed were dissolved in dimethyl sulfoxide (DMSO), with the corresponding solution added to 2% (v/v) final DMSO concentration. They were incubated for 5 min at 25 °C prior to addition of the substrate. The reaction was initiated by addition of 1, 60, and 5 mM D,L-glyceraldehyde (for AR, AKR1B10, and AKR1A1, respectively), and the decrease in optical density at 340 nm was monitored for 3 min at 25 °C in a UV-vis spectrophotometer (UV-1700 PharmaSpec, Shimadzu). The IC₅₀ value was determined to be the compound concentration that inhibits enzymatic activity by 50% and was calculated using the Grafit program (version 5.0; Erithacus Software). Values are given as the mean ± standard error of three experiments.

Isothermal titration calorimetry (ITC). ITC experiments were carried out with an ITC₂₀₀ Micro Titration Calorimeter (MicroCal), as described previously.^[43] The experiments were performed in three different buffer systems (10 mM HEPES, Tricine, and Tris, pH 8.0). Measurements were performed at 298.15 K with 3% (v/v) final DMSO concentration. An excess of NADP⁺ cofactor was added. The cell was filled with the solution containing the respective protein, NADP⁺, and DMSO. The syringe was filled with the respective inhibitor, NADP⁺, and DMSO. Final inhibitor concentrations were

between 300 and 1800 μM ; final protein concentrations ranged between 20 and 160 μM . Inhibitor solutions were titrated into a stirred cell containing the protein solution after a stable baseline was achieved. The protocol consisted of an initial injection of 0.5 μL to prevent any artefacts arising from the filling of the syringe (not used in data fitting), followed by injections of 1.5 μL , each spaced 240 s apart, until complete saturation of the enzyme binding site was achieved. Raw data were integrated and fitted with NITPIC^[44] and SEDPHAT^[45] plots of the thermograms and fitted curves were prepared using GUSI.^[46] Fitting a single-site-binding isotherm into the data led to the enthalpy of binding (ΔH°) and the dissociation constant (K_d) values. Measurements were performed in triplicate, except for the measurement of **4** with AR, which was done in duplicate because of the high amount of protein needed for the titration. The enthalpies were corrected for protonation effects, as described in the literature.^[27b,28] The heat of ionization ($\Delta H^\circ_{\text{ion}}$) of the buffer substances was taken from literature^[47] and plotted against the measured enthalpy ($\Delta H^\circ_{\text{obs}}$) in the corresponding buffer system. A line of best fit of the form $\Delta H_{\text{obs}} = \Delta H_{\text{bind}} + n \times \Delta H_{\text{ion}}$ was matched to the data points. The positive slope of the line, as obtained here, indicates how many protons are picked up. The negative slope indicates how many protons are released during the binding event. The interception point with the y -axis reflects the enthalpy corrected for the protonation effect. Mean values and standard deviations are shown in Table 2, with the measured values for $\Delta H^\circ_{\text{obs}}$ shown in Tables S1C and S1D in the SI. Example curves for the different measurements are shown in Figure S1 in the SI.

Western blot analysis. All cell lines were obtained from the American Type Culture Collection (ATCC) following the recommended protocols. Cells were collected from a confluent culture in a 25 cm^2 flask, using the standard method of trypsinization. After neutralizing the trypsin, the cell pellet was washed two times in phosphate-buffered saline (PBS) and was frozen at -20°C to facilitate cell lysis. Then, cells were thawed and resuspended with RIPA Buffer (Tris-HCl, pH 8.0, 1% IGEPAL CA-630, 0.5% sodium deoxycholate, 0.1% SDS, 10 mM sodium orthovanadate, 1 mM PMSF). 20 μg of cell extract and 200 ng purified recombinant AKR1B10 were loaded onto an SDS-PAGE, and separation was performed at 150 V for 90 min. Then, proteins were transferred for 1 h at 100 V onto a polyvinylidene difluoride (PVDF) membrane (Millipore). Once the transfer was completed, the membrane non-specific interaction sites were blocked by 5% skim milk solution in 0.1% Tween 20-Tris buffered saline (TTBS) for 90 min. The membrane was incubated for 90 min with rabbit primary polyclonal antibody against AKR1B10 (Bio-Rad) (diluted 1:2000 in 2.5% skim milk solution, 0.1% TTBS). Finally, the membrane was incubated for 90 min with goat peroxidase-conjugated secondary polyclonal antibody against rabbit antibody constant fraction (Bio-Rad), (diluted 1:5000 in 2.5% skim milk solution, 0.1% TTBS). The membrane was stained by a chemiluminescent method with luminol and hydrogen peroxide. A digital camera (Bio-Rad) was used to measure band intensities. β -actin was used for normalization of protein loading.

Intracellular sorbitol accumulation in ARPE-19 human retinal cells. Intracellular concentrations of sorbitol in ARPE-19 human retinal cells obtained from the ATCC were measured following the recommended protocol.^[15b] In brief, 1×10^7 cells were cultured in 2.5 mL of minimum essential medium (JRH Biosciences) supplemented with 0.5% fetal calf serum. Glucose (50 mM) was added to the culture medium to reproduce the intracellular hyperglycemic conditions of diabetes mellitus. The compounds to be assayed were dissolved in DMSO, and the corresponding solution was added to the

well. After a 16 h incubation at 37°C with 5% CO_2 , the accumulated sorbitol inside the cells was extracted by lysis with 8% perchloric acid and then neutralized with KOH. Quantification of sorbitol was carried out using a colorimetric method (*D*-sorbitol/xylitol, Boehringer Mannheim). The IC_{50} value for each test compound was determined as the compound concentration that inhibited sorbitol accumulation by 50%. Values are given as the mean of three experiments.

Cell viability assay. NCI-H460 and BEAS-2B cells were obtained from the ATCC and were incubated in RPMI 1640 and keratinocyte serum-free media (Life Technologies), respectively. All experiments were carried out in 96-well plates. Cellular densities of 2000 and 10000 cells cm^{-2} were reached for NCI-H460 and BEAS-2B, respectively. Seeded cells were incubated in a humidified atmosphere of 5% $\text{CO}_2/95\%$ air at 37°C for 24 h, prior to inhibitor treatment. Then, compounds were added to each well to reach the desired concentration with a final concentration of 0.2% DMSO (v/v), and cells were further incubated for 72 h. Cell viability was determined using the XTT Cell Proliferation Kit II (Roche), following the manufacturer's instructions. After adding XTT, cells were incubated for 90 min before reading the absorbance at 485 and 620 nm in a Wallace 1420 VICTOR³V multiplate reader (PerkinElmer Life Sciences). The absorbance at 620 nm was subtracted from the absorbance at 485 nm, and the resulting value was corrected for the control wells without cells. The percentage of viable cells was calculated by dividing this value by the result of wells treated with 0.2% DMSO. The results are shown as the mean \pm standard deviation of at least four experimental values.

Crystallization and structure determination

For the AR-NADP⁺-**3** complex, crystals were obtained by co-crystallization under previously published conditions:^[41,48] hanging drop method at 298 K, reservoir with 50 mM ammonium citrate, pH 5.0, 20% polyethylene glycol (PEG) 6000, with 5 mM of **3**. Neither co-crystallization nor soaking was successful for the AR-NADP⁺-**4** complex using these conditions. Later, co-crystals were obtained using the following conditions: 10 mM Tris-HCl, pH 8.0, 20% PEG 6000, with 5 mM of **4**. Regarding the AKR1B10 complexes, all crystals were obtained with the AKME2MU system (reductive lysine methylation plus K125R/V301L mutations), except for the methylated AKR1B10 holoenzyme. Co-crystals of the AKME2MU-NADP⁺-**4** (30 mM inhibitor) complex and of both mutant holoenzymes were obtained by the hanging drop vapor diffusion method at 298 K. The protein solution was mixed with an equal volume of precipitating solution consisting of 100 mM sodium cacodylate, pH 9.0, and 30% PEG 6000. The detailed protocol is given elsewhere.^[1] X-ray data were collected on the home source for the AKME2MU-NADP⁺-**4** complex, at the Swiss Light Source on the X06SA beamline for the AR-NADP⁺-**3** complex, and on X06DA for the methylated AKR1B10 holoenzyme and for AR-NADP⁺-**4** (for data collection statistics, see Table 3). All data sets were processed with the program HKL2000.^[49] The structures were solved by molecular replacement with Phaser^[50] (PDB model used in each case is indicated in Table 3), and finalized sets of atomic coordinates were obtained after iterative rounds of model modification with the program Coot^[34] and refinement with REFMAC5^[51] and PHENIX.^[52] Ligand coordinates and restraints were generated as previously reported^[1] or using eLBOW.^[53] The coordinate data for the structures were deposited, with PDB IDs as indicated in Table 3. Related figures were prepared with PyMOL (v 1.3; Schrödinger).

Docking simulations

Molecular docking to obtain the AKME2MU–NADP⁺–3 model was performed with the program AutoDock 4.2^[26] on a Linux workstation. Coordinates of **3** were taken from the AR cognate structure (PDB ID 4XZH). For the protein molecule, crystallographic ligands and water molecules were removed from the PDB file corresponding to the co-crystal of AKME2MU holoenzyme–JF0048–NADP⁺–3, in which the inhibitor could not be observed. Polar hydrogens were added by using the hydrogen module in AutoDock Tools (ADT), then Gasteiger united atom partial charges were assigned, except for NADP⁺, where the nicotinamide charge was kept positive.^[54] The remaining settings were the same as previously reported.^[55] All structures generated for the same compound were subjected to cluster analysis with a tolerance of 2.0 Å for an all-atom RMSD from a lower energy structure. Related figures were prepared with PyMOL (v 1.3; Schrödinger). Further docking studies were performed with the docking program FlexX,^[29] included in the LeadIT suite (BioSolveIT). Docking poses were selected following the same criteria as explained for AutoDock. The crystal structures with PDB IDs 1ZUA, 4JII, and 4GQ0 were used to obtain the corresponding protein conformers. The ligand and all crystallographic water molecules were removed. The compounds were subsequently docked.

Acknowledgements

The authors thank the Institut de Génétique et de Biologie Moléculaire et Cellulaire (IGBMC) Structural Genomics Platform staff (in particular, Dr. Catherine Birck, Dr. Alastair McEwen, and Pierre Poussin-Courmontagne). The crystallographic experiments were performed on the X06SA and X06DA beamlines at the Swiss Light Source synchrotron, Paul Scherrer Institut, Villigen, Switzerland. The authors thank Drs. Vincent Olieric and Takashi Tomizaki for their help on the beamlines and Dr. Marc Ruff for the X-ray data collection of the AR–NADP⁺–3 complex. This work was funded by the National Center for Scientific Research (CNRS), the Institut National de la Santé et de la Recherche Médicale (INSERM), the Université de Strasbourg, the Région Alsace, the Hôpital Civil de Strasbourg, Instruct (part of the European Strategy Forum of Research Infrastructures; ESFRI), the French Infrastructure for Integrated Structural Biology (FRISBI) (ANR-10-INSB-05-01), the Spanish Ministerio de Economía y Competitividad (BFU2011-24176), Generalitat de Catalunya (2009 SGR 795), the Fondation pour la Recherche Médicale (Code FRM: SPF20121226275) and the Bayer HealthCare 'Grants4Targets' program (entitled 'AKR1B10 as a molecular target for cancer control', 2009–2010). This work was supported by European Research Council (ERC) grant 268145–Drug-ProfilBind, kindly provided by the EU to G.K.

Keywords: aldose reductase · AKR1B10 · drug design · steric hindrance · buried water molecule

- [1] A. Cousido-Siah, F. X. Ruiz, A. Mitschler, S. Porté, Á. R. de Lera, M. J. Martín, S. Manzanaro, J. A. de La Fuente, F. Terwesten, M. Betz, G. Klebe, J. Farrés, X. Parés, A. Podjarny, *Acta Crystallogr. Sect. D* **2014**, *70*, 889–903.
[2] a) Z. Changjin in *Diabetes Mellitus—Insights and Perspectives* (Ed.: O. O. Oguntibeju), InTech—Open Access Company, **2013**, pp. 17–46; b) P. J.

- Oates, *Curr. Opin. Invest. Drugs* **2010**, *11*, 402–417; c) W. H. Tang, K. A. Martin, J. Hwa, *Front. Pharmacol.* **2012**, *3*, 87.
[3] a) K. V. Ramana, S. K. Srivastava, *Int. J. Biochem. Cell Biol.* **2010**, *42*, 17–20; b) R. Tammali, A. B. Reddy, A. Saxena, P. G. Rychahou, B. M. Evers, S. Qiu, S. Awasthi, K. V. Ramana, S. K. Srivastava, *Carcinogenesis* **2011**, *32*, 1259–1267.
[4] a) S. Fukumoto, N. Yamauchi, H. Moriguchi, Y. Hippo, A. Watanabe, J. Shibahara, H. Taniguchi, S. Ishikawa, H. Ito, S. Yamamoto, H. Iwanari, M. Hironaka, Y. Ishikawa, T. Niki, Y. Sohara, T. Kodama, M. Nishimura, M. Fukayama, H. Dosaka-Akita, H. Aburatani, *Clin. Cancer Res.* **2005**, *11*, 1776–1785; b) F. X. Ruiz, O. Gallego, A. Ardèvol, A. Moro, M. Domínguez, S. Álvarez, R. Álvarez, A. R. de Lera, C. Rovira, I. Fita, X. Parés, J. Farrés, *Chem.-Biol. Interact.* **2009**, *178*, 171–177; c) C. Wang, R. Yan, D. Luo, K. Watabe, D. F. Liao, D. Cao, *J. Biol. Chem.* **2009**, *284*, 26742–26748; d) E. Zeindl-Eberhart, S. Haraida, S. Liebmann, P. R. Jungblut, S. Lamer, D. Mayer, G. Jager, S. Chung, H. M. Rabes, *Hepatology* **2004**, *39*, 540–549.
[5] a) O. A. Barski, S. M. Tipparaju, A. Bhatnagar, *Drug Metab. Rev.* **2008**, *40*, 553–624; b) O. Gallego, O. V. Belyaeva, S. Porté, F. X. Ruiz, A. V. Stetsenko, E. V. Shabrova, N. V. Kostereva, J. Farrés, X. Parés, N. Y. Kedishvili, *Biochem. J.* **2006**, *399*, 101–109.
[6] a) O. Gallego, F. X. Ruiz, A. Ardèvol, M. Domínguez, R. Álvarez, A. R. de Lera, C. Rovira, J. Farrés, I. Fita, X. Parés, *Proc. Natl. Acad. Sci. USA* **2007**, *104*, 20764–20769; b) T. M. Penning, *Clin. Cancer Res.* **2005**, *11*, 1687–1690; c) A. M. Quinn, R. G. Harvey, T. M. Penning, *Chem. Res. Toxicol.* **2008**, *21*, 2207–2215; d) F. X. Ruiz, S. Porté, X. Parés, J. Farrés, *Front. Pharmacol.* **2012**, *3*, 58.
[7] J. Ma, R. Yan, X. Zu, J. M. Cheng, K. Rao, D. F. Liao, D. Cao, *J. Biol. Chem.* **2008**, *283*, 3418–3423.
[8] a) P. J. Oates, *Curr. Drug Targets* **2008**, *9*, 14–36; b) M. V. Reddy, P. Venkatapuram, M. R. Mallireddigari, V. R. Pallela, S. C. Cosenza, K. A. Robell, B. Akula, B. S. Hoffman, E. P. Reddy, *J. Med. Chem.* **2011**, *54*, 6254–6276.
[9] O. El-Kabbani, A. Podjarny, *Cell. Mol. Life Sci.* **2007**, *64*, 1970–1978.
[10] H. Steuber, A. Heine, A. Podjarny, G. Klebe, *J. Mol. Biol.* **2008**, *379*, 991–1016.
[11] a) B. Díez-Dacal, J. Gayarre, S. Gharbi, J. F. Timms, C. Coderch, F. Gago, D. Pérez-Sala, *Cancer Res.* **2011**, *71*, 4161–4171; b) S. Endo, T. Matsunaga, K. Kuwata, H. T. Zhao, O. El-Kabbani, Y. Kitade, A. Hara, *Bioorg. Med. Chem.* **2010**, *18*, 2485–2490; c) S. Endo, T. Matsunaga, H. Mamiya, C. Ohta, M. Soda, Y. Kitade, K. Tajima, H. T. Zhao, O. El-Kabbani, A. Hara, *Arch. Biochem. Biophys.* **2009**, *487*, 1–9; d) S. Endo, T. Matsunaga, M. Soda, K. Tajima, H. T. Zhao, O. El-Kabbani, A. Hara, *Biol. Pharm. Bull.* **2010**, *33*, 886–890; e) T. Matsunaga, S. Endo, M. Soda, H. T. Zhao, O. El-Kabbani, K. Tajima, A. Hara, *Biochem. Biophys. Res. Commun.* **2009**, *389*, 128–132; f) M. Soda, D. Hu, S. Endo, M. Takemura, J. Li, R. Wada, S. Ifuku, H. T. Zhao, O. El-Kabbani, S. Ohta, K. Yamamura, N. Toyooka, A. Hara, T. Matsunaga, *Eur. J. Med. Chem.* **2012**, *48*, 321–329; g) M. Takemura, S. Endo, T. Matsunaga, M. Soda, H. T. Zhao, O. El-Kabbani, K. Tajima, M. Inuma, A. Hara, *J. Nat. Prod.* **2011**, *74*, 1201–1206.
[12] a) L. Zhang, H. Zhang, Y. Zhao, Z. Li, S. Chen, J. Zhai, Y. Chen, W. Xie, Z. Wang, Q. Li, X. Zheng, X. Hu, *FEBS Lett.* **2013**, *587*, 3681–3686; b) L. Zhang, H. Zhang, X. Zheng, Y. Zhao, S. Chen, Y. Chen, R. Zhang, Q. Li, X. Hu, *ChemMedChem* **2014**, *9*, 706–709.
[13] F. X. Ruiz, A. Cousido-Siah, A. Mitschler, J. Farrés, X. Parés, A. Podjarny, *Chem.-Biol. Interact.* **2013**, *202*, 178–185.
[14] A. Cousido-Siah, F. X. Ruiz, I. Crespo, S. Porté, A. Mitschler, X. Parés, A. Podjarny, J. Farrés, *Chem.-Biol. Interact.* **2015**, *234*, 290–296.
[15] a) J. A. de La Fuente, S. Manzanaro, *Nat. Prod. Rep.* **2003**, *20*, 243–251; b) J. A. de La Fuente, S. Manzanaro, M. J. Martín, T. G. de Quesada, I. Reymundo, S. M. Luengo, F. Gago, *J. Med. Chem.* **2003**, *46*, 5208–5221; c) S. Manzanaro, J. Salva, J. A. de La Fuente, *J. Nat. Prod.* **2006**, *69*, 1485–1487.
[16] T. Kotani, Y. Nagaki, A. Ishii, Y. Konishi, H. Yago, S. Suehiro, N. Okukado, K. Okamoto, *J. Med. Chem.* **1997**, *40*, 684–694.
[17] O. M. Ali, H. H. Amer, A. A. H. Abdel-Rahman, *Synthesis* **2007**, 2823–2828.
[18] K. M. Bohren, C. E. Grimshaw, *Biochemistry* **2000**, *39*, 9967–9974.
[19] a) M. P. Blakeley, F. Ruiz, R. Cachau, I. Hazemann, F. Meilleur, A. Mitschler, S. Ginell, P. Afonine, O. N. Ventura, A. Cousido-Siah, M. Haertlein, A. Joachimiak, D. Myles, A. Podjarny, *Proc. Natl. Acad. Sci. USA* **2008**, *105*, 1844–1848; b) E. I. Howard, R. Sanishvili, R. E. Cachau, A. Mitschler, B. Chevrier, P. Barth, V. Lamour, M. Van Zandt, E. Sibley, C. Bon, D. Moras,

- T. R. Schneider, A. Joachimiak, A. Podjarny, *Proteins Struct. Funct. Bioinf.* **2004**, *55*, 792–804.
- [20] H. Steuber, A. Heine, G. Klebe, *J. Mol. Biol.* **2007**, *368*, 618–638.
- [21] C. Bissantz, B. Kuhn, M. Stahl, *J. Med. Chem.* **2010**, *53*, 5061–5084.
- [22] F. Ruiz, I. Hazemann, A. Mitschler, A. Joachimiak, T. Schneider, M. Karplus, A. Podjarny, *Acta Crystallogr. Sect. D* **2004**, *60*, 1347–1354.
- [23] D. W. Borhani, T. M. Harter, J. M. Petrash, *J. Biol. Chem.* **1992**, *267*, 24841–24847.
- [24] L. Zhang, H. Zhang, X. Zheng, Y. Zhao, S. Chen, Y. Chen, R. Zhang, Q. Li, X. Hu, *ChemMedChem* **2014**, *9*, 706–709.
- [25] Z. S. Derewenda, L. Lee, U. Derewenda, *J. Mol. Biol.* **1995**, *252*, 248–262.
- [26] G. M. Morris, R. Huey, W. Lindstrom, M. F. Sanner, R. K. Belew, D. S. Goodsell, A. J. Olson, *J. Comput. Chem.* **2009**, *30*, 2785–2791.
- [27] a) M. Stefek, M. Soltesova Prnova, M. Majekova, C. Rechlin, A. Heine, G. Klebe, *J. Med. Chem.* **2015**, *58*, 2649–2657; b) H. Steuber, P. Czodrowski, C. A. Sotriffer, G. Klebe, *J. Mol. Biol.* **2007**, *373*, 1305–1320.
- [28] F. Dullweber, M. T. Stubbs, D. Musil, J. Stürzebecher, G. Klebe, *J. Mol. Biol.* **2001**, *313*, 593–614.
- [29] M. Rarey, B. Kramer, T. Lengauer, G. Klebe, *J. Mol. Biol.* **1996**, *261*, 470–489.
- [30] D. Plewczyński, M. Łażniewski, R. Augustyniak, K. Ginalski, *J. Comput. Chem.* **2011**, *32*, 742–755.
- [31] C. A. Sotriffer, O. Kramer, G. Klebe, *Proteins Struct. Funct. Bioinf.* **2004**, *56*, 52–66.
- [32] a) G. Klebe, *Nat. Rev. Drug Discovery* **2015**, *14*, 95–110; b) R. Talhout, A. Villa, A. E. Mark, J. B. F. N. Engberts, *J. Am. Chem. Soc.* **2003**, *125*, 10570–10579.
- [33] N. Schneider, G. Lange, S. Hindle, R. Klein, M. Rarey, *J. Comput.-Aided Mol. Des.* **2013**, *27*, 15–29.
- [34] P. Emsley, B. Lohkamp, W. G. Scott, K. Cowtan, *Acta Crystallogr. Sect. D* **2010**, *66*, 486–501.
- [35] a) M. T. Barho, S. Oppermann, F. C. Schrader, I. Degenhardt, K. Elsässer, C. Wegscheid-Gerlach, C. Culmsee, M. Schlitzer, *ChemMedChem* **2014**, *9*, 2260–2273; b) N. T. Tzvetkov, S. Hinz, P. Küppers, M. Gastreich, C. E. Müller, *J. Med. Chem.* **2014**, *57*, 6679–6703.
- [36] a) E. Barratt, R. J. Bingham, D. J. Warner, C. A. Laughton, S. E. V. Phillips, S. W. Homans, *J. Am. Chem. Soc.* **2005**, *127*, 11827–11834; b) A. Biela, N. N. Nasief, M. Betz, A. Heine, D. Hangauer, G. Klebe, *Angew. Chem. Int. Ed.* **2013**, *52*, 1822–1828; *Angew. Chem.* **2013**, *125*, 1868–1876; c) L. Englert, A. Biela, M. Zayed, A. Heine, D. Hangauer, G. Klebe, *Biochim. Biophys. Acta Gen. Subj.* **2010**, *1800*, 1192–1202; d) S. W. Homans, *Drug Discovery Today* **2007**, *12*, 534–539; e) T. Young, R. Abel, B. Kim, B. J. Berne, R. A. Friesner, *Proc. Natl. Acad. Sci. USA* **2007**, *104*, 808–813.
- [37] K.-C. Chang, J. Ponder, D. V. LaBarbera, J. M. Petrash, *Invest. Ophthalmol. Visual Sci.* **2014**, *55*, 2853–2861.
- [38] R. Maccari, R. Ottanà, *J. Med. Chem.* **2015**, *58*, 2047–2067.
- [39] a) J. Ma, D. X. Luo, C. Huang, Y. Shen, Y. Bu, S. Markwell, J. Gao, J. Liu, X. Zu, Z. Cao, Z. Gao, F. Lu, D. F. Liao, D. Cao, *Int. J. Cancer* **2012**, *131*, E862–E871; b) R. Satow, M. Shitashige, Y. Kanai, F. Takeshita, H. Ojima, T. Jigami, K. Honda, T. Kosuge, T. Ochiya, S. Hirohashi, T. Yamada, *Clin Cancer Res.* **2010**, *16*, 2518–2528; c) R. Tammali, K. V. Ramana, S. S. Singhal, S. Awasthi, S. K. Srivastava, *Cancer Res.* **2006**, *66*, 9705–9713; d) W. Zhang, H. Li, Y. Yang, J. Liao, G.-Y. Yang, *Cancer Lett.* **2014**, *355*, 273–280.
- [40] J.-U. Peters, *J. Med. Chem.* **2013**, *56*, 8955–8971.
- [41] V. Lamour, P. Barth, H. Rogniaux, A. Poterszman, E. Howard, A. Mitschler, A. Van Dorsselaer, A. Podjarny, D. Moras, *Acta Crystallogr. Sect. D* **1999**, *55*, 721–723.
- [42] O. A. Barski, K. H. Gabbay, C. E. Grimshaw, K. M. Bohren, *Biochemistry* **1995**, *34*, 11264–11275.
- [43] a) C. Koch, A. Heine, G. Klebe, *J. Mol. Biol.* **2011**, *406*, 700–712; b) T. Petrova, H. Steuber, I. Hazemann, A. Cousido-Siah, A. Mitschler, R. Chung, M. Oka, G. Klebe, O. El-Kabbani, A. Joachimiak, A. Podjarny, *J. Med. Chem.* **2005**, *48*, 5659–5665.
- [44] S. Keller, C. Vargas, H. Zhao, G. Piszczek, C. A. Brautigam, P. Schuck, *Anal. Chem.* **2012**, *84*, 5066–5073.
- [45] H. Zhao, G. Piszczek, P. Schuck, *Methods* **2015**, *76*, 137–148.
- [46] C. A. Brautigam, The University of Texas Southwestern Medical Center, Dallas, TX, **2012**.
- [47] H. Fukada, K. Takahashi, *Proteins Struct. Funct. Bioinf.* **1998**, *33*, 159–166.
- [48] A. Cousido-Siah, T. Petrova, I. Hazemann, A. Mitschler, F. X. Ruiz, E. Howard, S. Ginell, C. Atmanene, A. Van Dorsselaer, S. Sanglier-Cianferani, A. Joachimiak, A. Podjarny, *Proteins Struct. Funct. Bioinf.* **2012**, *80*, 2552–2561.
- [49] Z. Otwinowski, W. Minor, *Macromol. Crystallogr. Part A* **1997**, *276*, 307–326.
- [50] A. J. McCoy, R. W. Grosse-Kunstleve, P. D. Adams, M. D. Winn, L. C. Storoni, R. J. Read, *J. Appl. Crystallogr.* **2007**, *40*, 658–674.
- [51] G. N. Murshudov, P. Skubak, A. A. Lebedev, N. S. Pannu, R. A. Steiner, R. A. Nicholls, M. D. Winn, F. Long, A. A. Vagin, *Acta Crystallogr. Sect. D* **2011**, *67*, 355–367.
- [52] P. D. Adams, P. V. Afonine, G. Bunkoczi, V. B. Chen, I. W. Davis, N. Echols, J. J. Headd, L. W. Hung, G. J. Kapral, R. W. Grosse-Kunstleve, A. J. McCoy, N. W. Moriarty, R. Oeffner, R. J. Read, D. C. Richardson, J. S. Richardson, T. C. Terwilliger, P. H. Zwart, *Acta Crystallogr. Sect. D* **2010**, *66*, 213–221.
- [53] N. W. Moriarty, R. W. Grosse-Kunstleve, P. D. Adams, *Acta Crystallogr. Sect. D* **2009**, *65*, 1074–1080.
- [54] J. De Ruyck, M. Famerée, J. Wouters, E. A. Perpète, J. Preat, D. Jacquemin, *Chem. Phys. Lett.* **2007**, *450*, 119–122.
- [55] S. Porté, F. X. Ruiz, J. Giménez, I. Molist, S. Alvarez, M. Domínguez, R. Alvarez, A. R. de Lera, X. Parés, J. Farrés, *Chem.-Biol. Interact.* **2013**, *202*, 186–194.

Received: September 1, 2015

Published online on November 9, 2015